

# Performance versus Robustness: Two-Prong Substructure Taggers for the LHC

---

**Disha Bhatia,<sup>1</sup> Reina Camacho,<sup>2</sup> Grigorios Chachamis,<sup>3</sup> Suman Chatterjee,<sup>1</sup> Frederic Dreyer,<sup>4</sup> Deepak Kar,<sup>5</sup> Peter Loch,<sup>6</sup> Ian Moult,<sup>7,8</sup> Ben Nachman,<sup>9</sup> Andreas Papaefstathiou,<sup>10</sup> Tousik Samui,<sup>11</sup> Andrzej Siodmok,<sup>12</sup> Gregory Soyez,<sup>13</sup> and Jesse Thaler<sup>4</sup>**

<sup>1</sup>*Tata Inst. of Fundamental Research, Mumbai, India*

<sup>2</sup>*Experimental Physics Department, CERN, CH-1211 Geneva 23, Switzerland*

<sup>3</sup>*Centro de Fisica Teorica y Matematicas, Madrid, Spain*

<sup>4</sup>*Center for Theoretical Physics, Massachusetts Institute of Technology, Cambridge, MA 02139, USA*

<sup>5</sup>*University of the Witwatersrand, Johannesburg, South Africa*

<sup>6</sup>*University of Arizona, Tucson, AZ 85721, USA*

<sup>7</sup>*Berkeley Center for Theoretical Physics, University of California, Berkeley, CA 94720, USA*

<sup>8</sup>*Theoretical Physics Group, Lawrence Berkeley National Laboratory, Berkeley, CA 94720, USA*

<sup>9</sup>*Physics Division, Lawrence Berkeley National Laboratory, Berkeley, CA 94720, USA*

<sup>10</sup>*Nikhef, Theory Group, Science Park 105, 1098 XG, Amsterdam, The Netherlands*

<sup>11</sup>*Indian Institute of Technology, Kanpure, India*

<sup>12</sup>*Theoretical Physics Department, CERN, CH-1211 Geneva 23, Switzerland*

<sup>13</sup>*IPhT, CEA Saclay, CNRS UMR 3681, F-91191 Gif-sur-Yvette, France*

*E-mail:* [loch@physics.arizona.edu](mailto:loch@physics.arizona.edu), [ianmoult@lbl.gov](mailto:ianmoult@lbl.gov), [bpnachman@lbl.gov](mailto:bpnachman@lbl.gov),  
[gregory.soyez@ipht.fr](mailto:gregory.soyez@ipht.fr), [jthaler@mit.edu](mailto:jthaler@mit.edu)

ABSTRACT: The ability to robustly identify, or “tag”, boosted hadronically-decaying resonances plays a central role at the LHC, both in searches for new physics, as well as for probing the Standard Model in extreme regions of phase space. While a variety of powerful and theoretically well-understood tagging approaches exist, their behavior in a realistic experimental environment is complicated by a number of issues including hadronization, underlying event, pile-up, and detector effects. In this paper, we perform a systematic study contrasting the robustness and performance of different theoretical approaches to designing jet substructure observables. These include the standard observables  $\tau_{21}$ ,  $D_2$ , and  $N_2$ , as well as various grooming strategies currently used by the LHC experiments. We also introduce a number of new observables, based on the idea of “dichroic ratios”, which are designed to simultaneously maximize both robustness and performance. For background QCD jets, we focus on the theoretical robustness to non-perturbative effects and the experimental robustness to detector effects. We discuss the different choices used by ATLAS and CMS, and we introduce reliable metrics for quantifying robustness and performance for substructure observables. Additionally, we study the dependence of taggers on the polarization of hadronically decaying  $W$  bosons, and identify strategies to perform polarimetry using the hadronic decay products. We conclude by making recommendations for future tagging strategies to ensure robust procedures based on sound theoretical organizing principles.

---

## Contents

<b>1</b>	<b>Introduction</b>	<b>1</b>
<b>2</b>	<b>Quantifying Performance and Robustness</b>	<b>3</b>
<b>3</b>	<b>Observable and Sample Definitions</b>	<b>7</b>
3.1	Jet Shape Observables	7
3.2	Grooming Techniques	9
3.3	Parton Shower Samples	11
<b>4</b>	<b>Theory Approaches to Robust Ratio Observables</b>	<b>11</b>
4.1	Review of the Dichroic Approach	12
4.2	New Dichroic Observables	14
4.3	Summary of Tagging Strategies	14
<b>5</b>	<b>Theory Robustness</b>	<b>16</b>
5.1	Hadronization	16
5.2	Underlying Event	20
5.3	Towards Improved Performance and Robustness for ATLAS and CMS	21
<b>6</b>	<b>Experimental Robustness</b>	<b>23</b>
6.1	Detector Models	23
6.2	Pile-Up Removal	26
6.3	Impact on Mass Resolution	26
<b>7</b>	<b>Polarization Dependence</b>	<b>28</b>
7.1	Performance Impact of Polarization	28
7.2	Tagging Longitudinal vs. Transverse Bosons	29
<b>8</b>	<b>Summary and Recommendations</b>	<b>30</b>

---

## 1 Introduction

With the ever-increasing dataset from the Large Hadron Collider (LHC), we are able to probe the Standard Model and search for physics beyond the Standard Model in increasingly extreme regions of phase space. Theoretically well-understood observables that are sensitive to such extreme regions of phase space are therefore playing an important role at the LHC. One

of the most exciting new approaches which has emerged at the LHC are tools from jet substructure, which allow for the identification of boosted hadronically-decaying particles within jets through a detailed study of their radiation patterns. Techniques from jet substructure have now been widely used for Standard Model measurements [1–12] as well as for searches for new physics [13–34].<sup>1</sup>

With the growing importance of jet substructure techniques, there has been a significant effort by both the theory and experimental communities to develop a more detailed understanding of the theoretical and experimental behavior of jet substructure observables. On the theory side, this has been pursued through explicit calculations [35–64], scaling arguments [65–67], and machine learning [68–74] approaches. On the experimental side, there have been detailed studies of the behavior of substructure observables in data, and their interplay with experimental realities, such as detector resolution and pile-up. Summaries can be found in Refs. [75–78], and Ref. [79] provides a review of recent theoretical and machine learning developments in jet substructure.

As a result of these efforts, there now exist a number of theoretically well-motivated jet substructure tools. For tagging hadronically-decaying  $W/Z/H$  bosons, which decay primarily to jets with two well-resolved prongs (also referred to as subjets), a variety of powerful two-prong taggers have been developed. Modern two-prong taggers typically consist of two ingredients: a groomer which removes low-energy contamination, and a jet shape observable which identifies the two-prong substructure. For jet shapes, it is well understood how to organize and study their behavior using power counting [66]. A variety of different classes of observables exist, for example the energy correlation functions [80–82] and  $N$ -subjettiness observables [83, 84], and their relation is understood. The behavior of groomers is also now well understood, and a number of groomers with favorable experimental and theoretical properties have been introduced [37, 85].

The theoretical understanding of the behavior of tagging observables is primarily based on perturbation theory, and it is therefore not always clear how this translates to experimental reality, due to the presence of hadronization, underlying event, detector effects, and pile-up. Indeed, the different LHC experiments have settled on different tagging combinations. For grooming, ATLAS using trimming [86] uses while CMS uses the modified Mass Drop Tagger (mMDT) [37] and its generalization, SoftDrop [85]. For jet shape observable, ATLAS uses  $D_2$  [54, 66], while CMS uses  $N$ -subjettiness ratio  $\tau_{2,1}$  [83, 84] or  $N_2$  [81] with DDT [87]. It is not clear whether these choices are driven by differences in the detectors, or an optimization with respect to different criteria, samples, or modeling. While detailed optimization must ultimately be performed by the experiments themselves, we believe that there is still much to be understood about the general organization and design of jet substructure observables.

In this paper, we perform a comprehensive study of performance and robustness for two-prong tagging techniques. To frame the study, we use a theoretical organization into

---

<sup>1</sup>More LHC studies using jet substructure can be found at <https://twiki.cern.ch/twiki/bin/view/AtlasPublic> and <http://cms-results.web.cern.ch/cms-results/public-results/publications/>.

different tagging strategies based on the idea of dichroic observables [88], which generalize ratio observables to allow hybrid combinations of groomed and ungroomed shapes. These contain as special instances all the familiar observables used by the experiments, as well as new observables, such as dichroic versions of the  $N_2$  and  $D_2$  observables. We therefore place the ATLAS and CMS strategies as specific examples of broader classes of theoretical approaches for tagging two-prong substructure, about which we can draw general conclusions regarding robustness and performance.

The goal of this study is to highlight the interplay between performance and robustness, and assess the choices made by the different LHC experiments. Here, “performance” refers to the tagging efficiency (for a given background rejection) in the absence of systematic uncertainties. This has been the primary way to assess jet substructure observables in the past, but it does not capture the full set of considerations needed to apply jet substructure techniques in practice. By contrast, “robustness” refers to modifications of the substructure observables as different physics aspects are added. In particular, we consider robustness to non-perturbative effects, namely hadronization and underlying event, robustness to detector effects, and robustness to pile-up radiation. We introduce metrics for quantifying robustness that we believe will be useful in future studies of jet substructure observables. This allows us to study the robustness of each tagging strategy in general, and the CMS and ATLAS approaches in particular. In all cases, we are able to identify observables with improved robustness and performance as compared with those currently used by the experiments.

As an additional aspect of this study, we also consider the robustness of the signal tagging efficiency to the polarization of the decaying boson. We show that while jet shape observables themselves are fairly robust to polarization, groomed mass cuts are not, so that the tagging efficiency depends strongly on the polarization. Furthermore, we propose that the momentum asymmetry of the subjects is a good discriminant between longitudinal and transverse polarizations, and can be used to perform polarimetry for boosted hadronic decays.

An outline of this paper is as follows. In Sec. 2, we define our metrics for studying robustness. We discuss the key physics issues that we would like to assess robustness to, both theoretical and experimental, and describe a chain of different steps in our simulation process such that each physics issue can be isolated and studied. In Sec. 3, we define all jet substructure observables that will be used throughout this paper, and provide details of our sample generation. In Sec. 4, we discuss theoretical approaches to designing robust two-prong taggers. We extend the approach of Ref. [88] and define several new dichroic observables formed from the energy correlation functions. In Sec. 5, we study the robustness of the observables to non-perturbative radiation both from hadronization and underlying event. In Sec. 6, we study robustness to detector and pile-up. In Sec. 7, we study the robustness of substructure observables to the polarization of a decaying  $W/Z$  boson, and introduce observables to distinguish polarized samples. We summarize our results in Sec. 8 and make a number of recommendations for future jet substructure studies.

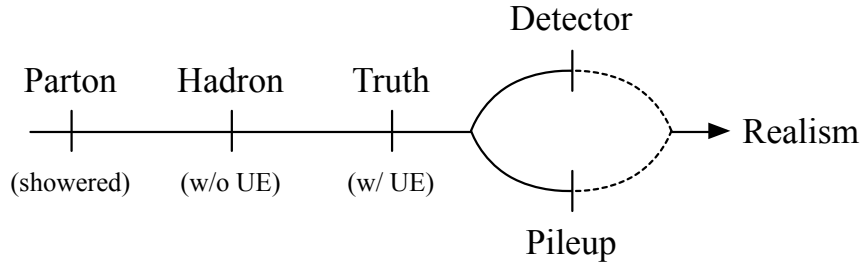


**Figure 1.** A summary of the different stages of physics considered in this study, from idealized parton-level events to fully realistic events including detector simulation and pile-up. This allows us to address robustness to physics at each stage. Detailed definitions of each stage, and the physics probes used, are given in the text.

## 2 Quantifying Performance and Robustness

The goal of this paper is to study the interplay between tagging performance and robustness for two-prong taggers. This requires a precise definition of the physics effects to which we are (or are not) robust, as well as a metric to quantify both performance and robustness.

Since we are able to generate pure signal and background samples, the tagging performance is straightforward to define using the signal and background efficiencies,  $\epsilon_S$  and  $\epsilon_B$ . In principle, we could evaluate the full receiver operating characteristic (ROC) curve relating  $\epsilon_B$  to  $\epsilon_S$ . For simplicity, we use the “tagging significance” as our metric for performance,

$$\epsilon = \frac{\epsilon_S}{\sqrt{\epsilon_B}}, \quad (2.1)$$

evaluated at a fixed signal efficiency, typically  $\epsilon_S = 0.4$ .

We will approach robustness by moving from an idealized partonic description to a complete detector simulation including pile-up; a “realistic” scenario representative of the LHC environment. This chain of realism is shown in Fig. 1, which illustrates the following stages:

- **Parton Level:** We define the parton level result as the perturbative distribution for the active-active scattering (i.e. we do not include possible perturbative contributions to the underlying event). While this can be defined in an analytic calculation, it is more difficult in the context of parton shower generators, since there is necessarily a cut-off that must be imposed between perturbative and non-perturbative physics. Only the complete result is physical, and intermediate results should be interpreted with care. Nevertheless, to have some measure of the impact of non-perturbative effects, we will define parton level as generated by a parton shower generator with all hadronization effects turned off. We use PYTHIA 8 [89, 90] as our baseline generator, leaving a study of additional generators to future work.

- **Hadron Level:** We define the hadron level result as including hadronization in the shower, but not including any effects from the underlying event.
- **Truth Level:** We define truth level as the hadronized result including the underlying event as implemented in an event generator. Truth level therefore represents a complete hard scattering process in a hadron-hadron collider in isolation.

At this stage our chain bifurcates, and we separately consider two different effects:

- **Detector Level:** Detector-level results are defined as truth level events passed through a detector simulation as implemented by TowerGrid. See Sec. 6.1 for details of the detector simulation.
- **Pile-up Level:** Due to the high pile-up environment of the LHC, we include in our study also the effects of uncorrelated proton interactions. We have done this separately from detector effects to be able to isolate and study the physics effects arising from pile-up and pile-up subtraction schemes. Our pile-up subtraction schemes are described in Sec. 6.2.
- **Full Realism:** In the final stage of realism, we consider events with pile-up at detector level. These represent, to the level that we can consider in this paper, realistic events as seen by the experiments at the LHC.

Comparing the differences as we progress step by step through this sequence allows us to address at each stage the robustness to distinct physics issues, and we hope that our segmentation is sufficiently fine that we have a comprehensive view of robustness. In particular, the different steps in the chain allow us to study robustness to the following physics:

- **Parton  $\rightarrow$  Hadron:** Changes in the distribution from parton level to hadron level probe non-perturbative physics associated with hadronization. For many event shapes, hadronization corrections can be given a field-theoretic definition in terms of a matrix element whose symmetry properties can be used to prove basic results. Ultimately, such corrections cannot be computed from first principles and must be included through models, such as those included in parton shower generators, or through shape functions in analytic calculations [91–97]. To have the best theoretical control and understanding of jet substructure observables, it is therefore desirable that their performance is robust to the effects of hadronization.
- **Hadron  $\rightarrow$  Truth:** Changes in the distribution from hadron level to truth level probe the impact of the underlying event, namely the physics associated with interactions of the colliding protons and their remnants. Such contributions are in principle both perturbative and non-perturbative. They are poorly understood theoretically, and it is currently not known how to treat them systematically, or define them field theoretically. It has been found empirically that the effects of underlying event are well modeled

by a shape function [98], although the theoretical justification for this is not clear. Other simple theoretical models from which intuition can be gained have been proposed Ref. [99]. The underlying event is implemented in parton shower event generators using models which are tuned to data, and we take these models as our definition of the underlying event. Due to this lack of theoretical understanding, as well as the fact that radiation from the underlying event is typically not associated with the physics that we are interested in probing, it is desirable that jet substructure observables be robust to the underlying event.

- **Truth  $\rightarrow$  Detector:** Since we are ultimately interested in using jet substructure in experiments, the behavior of the detectors plays an essential role. The finite energy and spatial resolution of the detectors ultimately degrades the behavior of the observables. Furthermore, the detector response must be unfolded, and is therefore difficult to compute analytically, or to include to higher accuracy. Therefore, both for performance, and calculability it is desirable that jet substructure observables are robust to detector effects.
- **Truth  $\rightarrow$  Pile-up:** Finally, due to the high pile-up environment of the LHC, significant soft radiation can contaminate jet substructure observables. Since this radiation is not correlated with the underlying hard scattering process, it is not associated with the physics of interest, and therefore can only act to degrade the performance. Furthermore, it is difficult to model in an analytic calculation. While techniques exist to mitigate pile-up, as were reviewed in Sec. 6.2, it is desirable that the substructure observables used are as robust as possible to pile-up contamination.

We will classify the first two of these as “Theory” issues, which will be discussed in Sec. 5, while the second two are classified as “Experimental” issues, and will be discussed in Sec. 6. This decomposition is of course somewhat arbitrary, since a coherent understanding involving the complete chain is required. However, this decomposition was chosen such that the “Theory” issues cover an idealized hadronic collision in isolation.

To compare the robustness to a particular step in this chain for different observables, we must introduce a metric. There is of course a high degree of arbitrariness in the definition of the metric. For example, one could base the metric on the shape of the signal or background distribution. Since we are ultimately interested in the performance of the observable, however, we introduce a metric which is based on the modification of the ROC curve. Consider a reference stage (unprimed) and a modified stage (primed); in the case of hadronization, the reference stage would be the hadron level and the modified stage would be the parton level. We first calculate the cut on the jet shape  $v_{\text{cut}}$  that yields a fixed signal efficiency  $\epsilon_S$  for the reference stage. We then compute the reference stage background efficiency  $\epsilon_B$  from that  $v_{\text{cut}}$ , as well as the modified stage signal and background efficiencies  $\epsilon'_S$  and  $\epsilon'_B$ . We can then



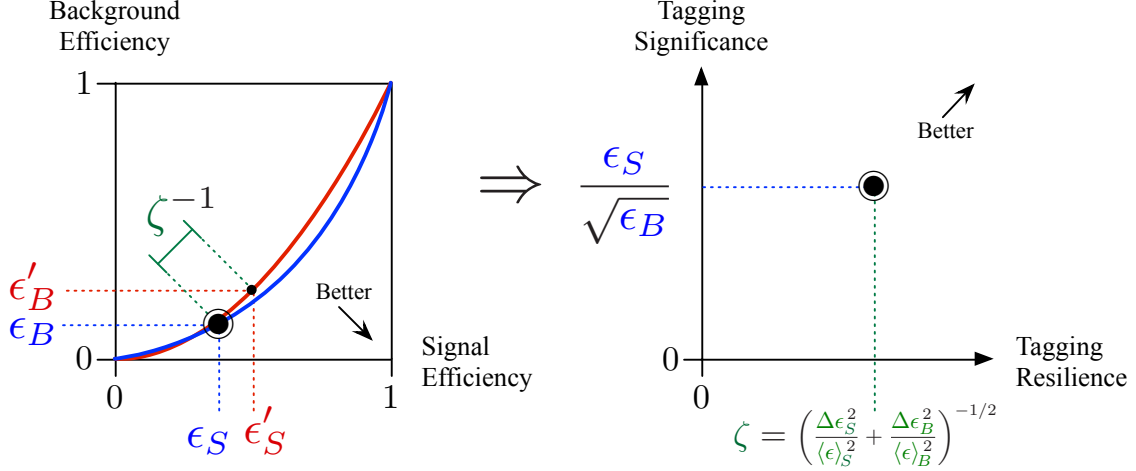


**Figure 2.** An illustration of the resilience metric  $\zeta$  used throughout the text to quantify robustness. In the left panel, we illustrate graphically  $\zeta$  as the change in ROC curve to a particular aspect of the underlying physics. In the right panel, we illustrate the tagging resilience vs. tagging performance plane which we will use to graphically illustrate our results. A simultaneously robust and performant tagger lives in the upper right hand corner of this space

defined a measure of robustness, which we refer to as resilience,  $\zeta$ , as

$$\zeta = \left( \frac{\Delta\epsilon_S^2}{\langle\epsilon\rangle_S^2} + \frac{\Delta\epsilon_B^2}{\langle\epsilon\rangle_B^2} \right)^{-1/2}, \quad (2.2)$$

where

$$\Delta\epsilon_{S,B} = \epsilon_{S,B} - \epsilon'_{S,B}, \quad (2.3)$$

$$\langle\epsilon\rangle_{S,B}^2 = \frac{1}{2} (\epsilon_{S,B} + \epsilon'_{S,B}). \quad (2.4)$$

This approach gives an estimate of how much our signal and background efficiencies have changed, for a given set of cuts, when going from one stage to another.

The meaning of  $\zeta$  is illustrated in Fig. 2, where larger values of  $\zeta$  correspond to improved robustness. Because we anchor to a fixed  $v_{\text{cut}}$ , this method can even detect a uniform shift in both the signal and background distributions (even though such a shift would not change the ROC curve). We therefore believe that  $\zeta$  provides a reliable metric for assessing the robustness of the tagger. When presenting our results, we characterize observables in the plane of  $\epsilon$  versus  $\zeta$ , with better observables being in the upper-right corner. We find that this allows us to synthesize the information about a large number of observables in a compact manner. A similar metric and presentation style was used in Ref. [88] to study robustness to non-perturbative effects. In addition to showing plots of the  $\epsilon$ - $\zeta$  plane, we will occasionally

also show the modification of the distribution itself to provide additional insight into the robustness of the observables.

It is important to emphasize that it is impossible to completely characterize an optimal observable, particularly as jet substructure observables are being used for increasingly specific purposes. We hope that the issues that we have chosen to focus on are representative of the issues that will be important for a broad range of applications. Other aspects, such as the robustness of the substructure observable distributions to changes in the jet mass or  $p_T$  cuts, which are important for certain recent applications of jet substructure [100–105], and have received recent interest [106–108], are beyond the scope of the current project. However, it would be interesting to investigate them using similar techniques.

### 3 Observable and Sample Definitions

In this section, we define all the observables that will be studied throughout this paper. This includes both the jet substructure shape observables and the grooming procedures. We also present the details of our sample generation.

#### 3.1 Jet Shape Observables

The jet shape observables that we will consider are formed from ratios of the energy correlation functions [80, 81] or the  $N$ -subjettiness observables [83, 84]. The  $N$ -subjettiness observables are defined as [83, 84, 109]

$$\tau_N^{(\beta)} = \frac{1}{p_{TJ}} \sum_{1 \leq i \leq n_J} p_{Ti} \min \left\{ R_{i1}^\beta, \dots, R_{iN}^\beta \right\} . \quad (3.1)$$

Here  $p_{TJ}$  is the  $p_T$  of the jet,  $p_{Ti}$  is the  $p_T$  of particle  $i$ , and the sum is over all particles in the jet. The minimum is over the longitudinally-boost-invariant angle

$$R_{iJ}^2 = (\phi_i - \phi_J)^2 + (y_i - y_J)^2 , \quad (3.2)$$

between the particle  $i$  and the axis  $J$ .

Implicit in the definition of the  $N$ -subjettiness observable in Eq. 3.1 is the definition of the axes  $n_i$ . While their placement is unambiguous (up to power corrections) in the limit of resolved substructure, an algorithmic definition is required to determine their behavior in the unresolved limit. Two main approaches have been used for defining the axes. The first approach is to define the  $N$ -subjettiness axes as the axes found using an exclusive jet clustering algorithm. The second approach is to minimize the sum in Eq. 3.1 over possible light-like axes  $n_i$ . In this paper, we defined the axes using subjects obtained by reclustering the jet, with choices motivated by the studies in Refs. [55, 110]. For  $\beta = 1$ , we recluster using the  $k_t$  algorithm [111] with the winner-take-all recombination scheme [112]. For  $\beta = 2$ , we use the generalized  $k_t$  algorithm [113] with  $p = 1/2$ .

For two-prong tagging, the relevant observable is the ratio [83]

$$\tau_{2,1}^{(\beta)} \equiv \frac{\tau_2^{(\beta)}}{\tau_1^{(\beta)}}. \quad (3.3)$$

For a jet with a well resolved two-prong structure, we have  $\tau_{2,1}^{(\beta)} \ll 1$ , while for a jet without a well resolved substructure, we have  $\tau_{2,1}^{(\beta)} \sim 1$ . This observable has been extensively used at the LHC. It has been calculated to LL accuracy [55], and the effects of the axis definition on the perturbative behavior have been studied at NLO [114].

The second class of observables that we will consider are based on the energy correlation functions [80, 81]. Instead of correlating particles with axes, as is done for  $N$ -subjettiness, the idea of the energy correlation functions is to correlate  $n$ -tuples of particles. In discussing the energy correlation functions, it is convenient to work with dimensionless observables, written in terms of an energy fraction variable,  $z_i$ , and an angular variable,  $R_{ij}$ :

$$z_i \equiv \frac{p_{Ti}}{\sum_{j \in \text{jet}} p_{Tj}}, \quad R_{ij}^2 = (\phi_i - \phi_j)^2 + (y_i - y_j)^2, \quad (3.4)$$

where  $p_{Ti}$ ,  $\phi_i$ , and  $y_i$  are the transverse momentum, azimuthal angle, and rapidity of particle  $i = 1, \dots, n_J$ , respectively. The generalized energy correlation function is defined as

$${}_v e_n^{(\beta)} = \sum_{1 \leq i_1 < i_2 < \dots < i_n \leq n_J} z_{i_1} z_{i_2} \dots z_{i_n} \prod_{m=1}^v \min_{s < t \in \{i_1, i_2, \dots, i_n\}}^{(m)} \left\{ R_{st}^\beta \right\}, \quad (3.5)$$

where  $\min^{(m)}$  denotes the  $m$ -th smallest element in the list. For a jet consisting of fewer than  $n$  particles,  ${}_v e_n$  is defined to be zero. More explicitly, the three arguments of the generalized energy correlation functions are as follows:

- The subscript  $n$ , which appears to the right of the observable, denotes the number of particles to be correlated.
- The subscript  $v$ , which appears to the left of the observable, denotes the number of pairwise angles entering the product. By definition, we take  $v \leq \binom{n}{2}$ , and the minimum then isolates the product of the  $v$  smallest pairwise angles.
- The angular exponent  $\beta > 0$  can be used to adjust the weighting of the pairwise angles.

In this paper, we use the 2-point energy correlation function,

$${}_1 e_2^{(\beta)} \equiv e_2^{(\beta)} = \sum_{1 \leq i < j \leq n_J} z_i z_j R_{ij}^\beta, \quad (3.6)$$

as well as the 3-point correlators,

$$\begin{aligned}
{}_1e_3^{(\beta)} &= \sum_{1 \leq i < j < k \leq n_J} z_i z_j z_k \min \left\{ R_{ij}^\beta, R_{ik}^\beta, R_{jk}^\beta \right\} , \\
{}_2e_3^{(\beta)} &= \sum_{1 \leq i < j < k \leq n_J} z_i z_j z_k \min \left\{ R_{ij}^\beta R_{ik}^\beta, R_{ij}^\beta R_{jk}^\beta, R_{ik}^\beta R_{jk}^\beta \right\} , \\
e_3^{(\beta)} \equiv {}_3e_3^{(\beta)} &= \sum_{1 \leq i < j < k \leq n_J} z_i z_j z_k R_{ij}^\beta R_{ik}^\beta R_{jk}^\beta .
\end{aligned} \tag{3.7}$$

A number of powerful 2-prong discriminants have been formed from the energy correlation functions [66, 67, 80, 81]. Here, we will focus on the observables

$$M_2^{(\beta)} = \frac{{}_1e_3^{(\beta)}}{{}_2e_2^{(\beta)}}, \quad N_2^{(\beta)} = \frac{{}_2e_3^{(\beta)}}{({}_2e_2^{(\beta)})^2}, \quad D_2^{(\beta)} = \frac{{}_3e_3^{(\beta)}}{({}_2e_2^{(\beta)})^3}, \tag{3.8}$$

each of which probes the correlations between particles within the jet in a slightly different manner. For a detailed discussion, see Ref. [81]. The  $N_2$  observable has been used by CMS, and the  $D_2$  observable has been used by ATLAS. The  $M_2$  observable is expected to have worse performance, except in particular scenarios, but we include it since it provides an example of a remarkably robust observable.

Beyond their discrimination power, these observables have nice theoretical properties. First, since they can be written as a sum over particles in the jet without reference to external axes, they are automatically “recoil-free” [80, 112, 115–117]. Second, since they have well-defined behavior in various soft and collinear limits, they are amenable to resummed calculations; in Ref. [54],  $D_2$  was calculated to next-to-leading-logarithmic (NLL) accuracy in  $e^+e^-$  for both signal (boosted  $Z$ ) and background (QCD) jets, and this was extended in Refs. [63, 64] to a hadron-collider environment by exploiting the simplifying properties of grooming.

### 3.2 Grooming Techniques

Groomers, which remove wide angle soft radiation and contamination from a jet, also play an important role in two-prong tagging. While a variety of different grooming approaches have been defined [37, 38, 86, 118–120], we will focus on the SoftDrop/mMDT family, which is the most theoretically well understood, as well as trimming [86], which is used by the ATLAS experiment. In this subsection, we review the definition of the SoftDrop/mMDT and trimming algorithms and their parameters.

Starting from a jet identified with an IRC safe jet algorithm (such as anti- $k_t$  [121]), the SoftDrop algorithm is defined using Cambridge/Aachen (C/A) reclustering [122–124]. For  $\beta = 0$ , SoftDrop is equivalent to the mMDT [37]. For this reason, we will often use the two names interchangeably. The SoftDrop algorithm proceeds as follows:

1. Recluster the jet using the C/A clustering algorithm, producing an angular-ordered branching history for the jet.

2. Step through the branching history of the reclustered jet. At each step, check the SoftDrop condition

$$\frac{\min[p_{Ti}, p_{Tj}]}{p_{Ti} + p_{Tj}} > z_{\text{cut}} \left( \frac{R_{ij}}{R} \right)^\beta. \quad (3.9)$$

Here,  $z_{\text{cut}}$  is a parameter defining the scale below which soft radiation is removed. If the SoftDrop condition is not satisfied, then the softer of the two branches is removed from the jet. This process is then iterated on the harder branch.

3. The SoftDrop procedure terminates once the SoftDrop condition is satisfied.

Given a jet that has been groomed with the SoftDrop procedure, we can then measure any IRC-safe observable on this jet and it is IRC safe. The severity of the SoftDrop grooming can be adjusted by tuning the parameters  $z_{\text{cut}}$  and  $\beta$ . Larger values of  $z_{\text{cut}}$  groom away more radiation within the jet for a fixed value of  $\beta$ . On the other hand, as  $\beta$  is increased, the grooming becomes less severe. Typical values of  $z_{\text{cut}}$  are around 0.1, while typical values of  $\beta$  are between 0 and 2.

Associated with the SoftDrop algorithm, in Sec. 7 we will study the observable  $z_g$  as a means for performing polarimetry. The  $z_g$  observable is also referred to as the groomed momentum fraction, and is defined as

$$z_g = \frac{\min[p_{Ti}, p_{Tj}]}{p_{Ti} + p_{Tj}} \quad (3.10)$$

for the first declustering that satisfies the SoftDrop criteria. This observable probes the momentum sharing between the two prongs in the jet. For  $\beta \geq 0$ , this observable is Sudakov safe [125, 126] on QCD jets.

In addition to SoftDrop/mMDT, we also consider the trimming algorithm, since it is used by the ATLAS collaboration. Starting from a jet of radius  $R$  identified with an IRC-safe jet algorithm, trimming is defined by the following procedure:

1. Recluster the jet into subjets of radius  $R_{\text{sub}}$ .
2. Eliminate from the jet all particles in subjets that satisfy  $p_{T,\text{subjet}} > z_{\text{cut}} p_{T,\text{jet}}$ .
3. The trimmed jet is then defined to consist of the remaining particles.

Trimming has been experimentally shown to be a powerful grooming algorithm, and it exhibits excellent mass resolution. That said, trimming is known to suffer from non-global logarithms [127], and does not have a smooth spectrum as a function of the trimmed mass. The trimmed mass was analytically calculated in Ref. [37]. The trimming parameters used by ATLAS are  $R_{\text{sub}} = 0.2$ ,  $z_{\text{cut}} = 0.05$ , and the  $k_T$  algorithm is used to perform the reclustering.

Model	Production couplings	Decay couplings	Decay helicity amplitudes
$2_b^+$	$g_1 = 1$	$g_5 = 1$	$f_{00} = 0.98$
$2_m^+$	$g_1 = 1$	$g_1 = g_5 = 1$	$f_{00} = 0.08, f_{+-} = f_{-+} = 0.46$

**Table 1.** A description of the production and decay constants used to produced the polarized  $W$  samples used in this studies.

### 3.3 Parton Shower Samples

For our QCD background jet samples we generated  $pp \rightarrow$  dijets in PYTHIA 8.226 [89, 90] with tune 4C. Samples were generated with hadronization off (parton level), with hadronization on but underlying event off (hadron level), and with hadronization and underlying event on (truth level). Pile-up was included by superimposing uncorrelated minimum bias events, which are also generated in PYTHIA. Details of our pile-up removal strategies will be described in Sec. 6.2.

For our polarized  $W$  samples, we considered a  $gg$  produced resonance,  $X$ , that decays to a pair of polarized  $W$  bosons. This kind of resonance decaying to longitudinally polarized  $W$ s appear in warped extra-dimensional models, where the Standard Model fields propagate in the bulk. On the other hand, models with graviton-like tensors with minimal couplings yield only transversely polarized  $W$  bosons. They were produced with the JHUGEN 3.1.8 [128, 129] generator, interfaced with PYTHIA 8 [90] for parton showering including the effect of hard gluon radiation. A resonance width of 1% was chosen. Table 1 shows the coupling values used to generate the polarised  $W$  samples (see also Ref. [128] for more information).

## 4 Theory Approaches to Robust Ratio Observables

The observables defined in Sec. 3.1 are designed to distinguish boosted bosons from QCD jets using the detailed structure of the radiation within the jets. From this perspective, it is then immediately clear that there will be an interplay between performance and robustness. By using a maximal amount of radiation within the jet, the maximal information is available to identify the origin of the jet. However, an increased sensitivity to radiation also means an increased sensitivity to contamination, both theoretically from non-perturbative hadronization effects and underlying event, as well as experimentally from pile-up. It also introduces sensitivity to the experimental reconstruction of soft momenta in the event. On the other hand, a tight grooming procedure, which removes radiation from within the jet, is expected to reduce the ability to distinguish boosted bosons from QCD jets.

In this section, we introduce a classification of different tagging strategies which will be an organizing framework for our study of robustness and performance. This organization will be based on the idea of dichroic observables [88], which are ratio observables constructed from combinations of groomed and ungroomed observables. In Sec. 4.1, we review the physics of the dichroic approach for the example of the  $\tau_{21}$  observable. In Sec. 4.2, we generalize the dichroic construction to energy correlation function based observables and give definitions

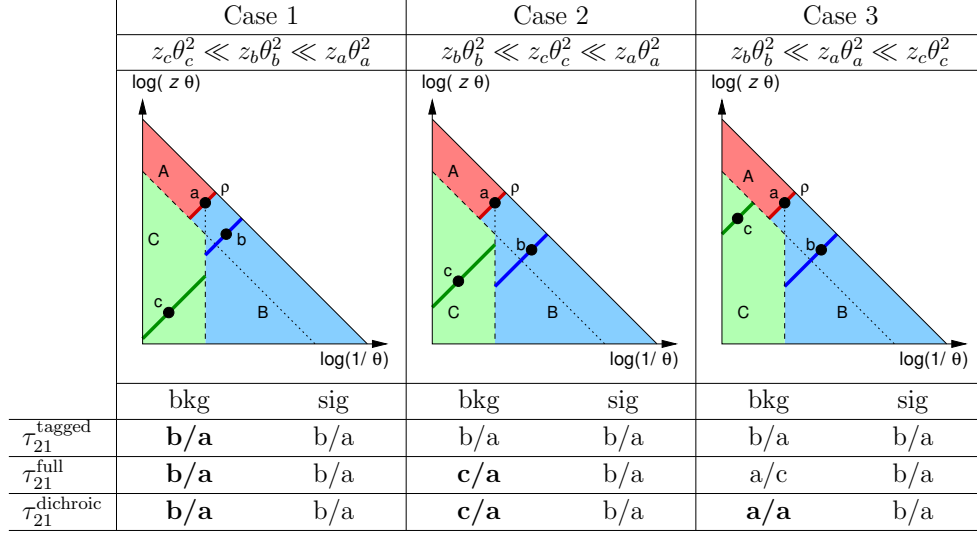


**Figure 3.** Lund diagrams depicting the three possible kinematic configurations for  $\tau_{21}$  with a cut on the mMDT/SoftDropped mass. A detailed explanation is provided in the text. Figure taken from Ref. [88].

of dichroic  $N_2$ ,  $D_2$  and  $M_2$  observables. This allows us to have multiple concrete examples of observables for each of our general tagging strategies. Then, in Sec. 4.3 we present the complete set of tagging strategies that we will consider in this work, including the different parameters we will scan within each general class.

#### 4.1 Review of the Dichroic Approach

In Ref. [88], it was proposed that in addition to considering the standard  $\tau_{21}$  observable and its groomed counterpart, one should also consider a mixed version, with a groomed denominator, and an ungroomed numerator. This observable was termed “dichroic”, since different levels of grooming are sensitive to different color structures. More explicitly, Ref. [88] considered the three observables:

$$\tau_{21} = \frac{\tau_2}{\tau_1}, \quad \tau_{21}^{\text{groomed}} = \frac{\tau_2^{\text{groomed}}}{\tau_1^{\text{groomed}}}, \quad \tau_{21}^{\text{dichroic}} = \frac{\tau_2}{\tau_1^{\text{groomed}}}, \quad (4.1)$$

and argued that the dichroic combination was optimal for performance, while also increasing the robustness to non-perturbative contamination. Here we briefly summarize the motivation for the dichroic observable, following closely the presentation in Ref. [88]. Readers interested in a more detailed discussion of the dichroic approach, including perturbative calculations, are referred to Ref. [88].

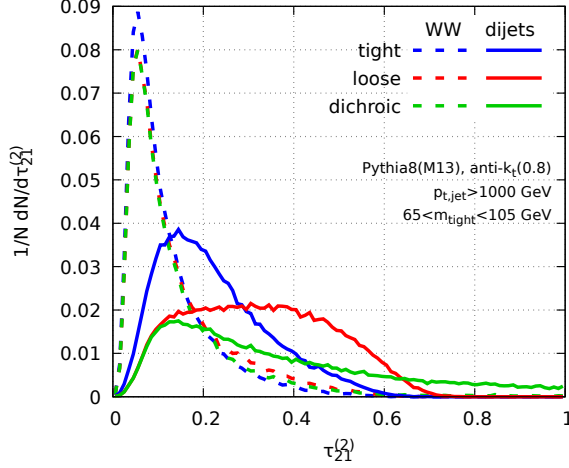


**Figure 4.** Distributions of the tight, loose, and dichroic  $\tau_{21}$  observables with a cut on the mMDT/SoftDropped mass. The dichroic approach offers considerably improved performance as compared with the tight grooming, almost preserving the performance of the loose grooming at high signal purity. Figure taken from Ref. [88].

Using the Lund diagrams [130] in Fig. 3, we can give a simple argument for the optimal performance of the dichroic observables by considering the behavior in each of the three regions:

- Case 1:  $z_c\theta_c^2 \ll z_b\theta_b^2 \ll z_a\theta_a^2$ : All definitions of  $\tau_{21}$  give the same result, and are therefore equivalent.
- Case 2:  $z_b\theta_b^2 \ll z_c\theta_c^2 \ll z_a\theta_a^2$ :  $\tau_{21}^{\text{groomed}} = z_b\theta_b^2/z_a\theta_a^2 \ll z_c\theta_c^2/z_a\theta_a^2 = \tau_{21} = \tau_{21}^{\text{dichroic}}$ , showing that the groomed version performs suboptimally in this region of phase space.
- Case 3:  $z_b\theta_b^2 \ll z_a\theta_a^2 \ll z_c\theta_c^2$ :  $\tau_{21}^{\text{dichroic}} = 1$ , and therefore  $\tau_{21}^{\text{dichroic}} \gg \tau_{21}$ ,  $\tau_{21}^{\text{dichroic}} \gg \tau_{21}^{\text{groomed}}$ .

Since in all cases we have  $\tau_{21} = z_b\theta_b^2/z_a\theta_a^2$  for the signal, this shows that the dichroic ratio is optimal. The identical argument can be reversed to show that using a groomed numerator and an ungroomed denominator is not optimal.

These benefits of the dichroic approach can also be illustrated in a less abstract manner by considering the distributions of the observables after aggressive grooming (tight), moderate grooming (loose), and in the dichroic approach. This is shown in Fig. 4 for the particular case of  $\tau_{21}$ . Considerable performance is lost in going from loose to tight grooming, since the background distribution is pushed to lower values of  $\tau_{21}$ . For the dichroic observable, by contrast, the behavior of the loose and dichroic observables is identical at small values of  $\tau_{21}$ , leading to improved performance. Indeed, at high signal purity, the performance of



Observable	Numerator	Denominator
$M_2$	${}_1e_3$	$e_2$
$N_2$	${}_2e_3/e_2$	$e_2$
$D_2$	$e_3/e_2^2$	$e_2$
$\tau_{21}$	$\tau_2$	$\tau_1$

**Table 2.** Definitions of the numerators and denominators for the different jet substructure observables.

the dichroic observable is nearly equal to that with loose grooming. Since the dichroic ratio observable uses a partially groomed observable, however, it is less sensitive to non-perturbative effects due to hadronization. It therefore represents an interesting new class of observable to consider.

## 4.2 New Dichroic Observables

It is straightforward to extend the dichroic definition from  $N$ -subjettiness ratios to observables formed from the energy correlation functions. For  $\tau_{21}$  it is immediately clear what the numerator and denominator of the observable are, however, this is initially less obvious for the energy correlation function based observables that have a more complicated structure. Here, we define the dichroic variants of the  $M_2$ ,  $N_2$  and  $D_2$  by isolating a single factor of a mass like observable ( $e_2$ ) as the denominator, and defining the remainder of the observable as the numerator. The definitions of the variants of the  $M_2$ ,  $N_2$  and  $D_2$  observables are then

$$M_2 = \frac{{}_1e_3}{e_2}, \quad M_2^{\text{groomed}} = \frac{{}_1e_3}{e_2^{\text{groomed}}}, \quad N_2^{\text{dichroic}} = \frac{{}_1e_3}{e_2^{\text{groomed}}}, \quad (4.2)$$

$$N_2 = \frac{({}_2e_3/e_2)}{e_2}, \quad N_2^{\text{groomed}} = \frac{({}_2e_3/e_2)^{\text{groomed}}}{e_2^{\text{groomed}}}, \quad N_2^{\text{dichroic}} = \frac{({}_2e_3/e_2)}{e_2^{\text{groomed}}}, \quad (4.3)$$

and

$$D_2 = \frac{(e_3/e_2^2)}{e_2}, \quad D_2^{\text{groomed}} = \frac{(e_3/e_2^2)^{\text{groomed}}}{e_2^{\text{groomed}}}, \quad D_2^{\text{dichroic}} = \frac{(e_3/e_2^2)}{e_2^{\text{groomed}}}. \quad (4.4)$$

The above prescription is most easy to see for the  $N_2$  observable. In the two-prong limit, the combination  ${}_2e_3/e_2$  reduces to  $\tau_2$ , and therefore the dichroic  $N_2$  ratio behaves similarly to the dichroic  $\tau_{21}$  ratio.

## 4.3 Summary of Tagging Strategies

The tagging strategies we consider can be put into the general form of a (groomed) mass cut ( $m$ ) followed by a cut on a two-prong tagging observable, which takes the form

$$\mathcal{O} = \frac{\text{3-particle observable}}{\text{2-particle (mass) observable}} \equiv \frac{n}{d}. \quad (4.5)$$

Notation: $m \otimes \frac{n}{d}$	$m$ (mass)	$n$ (numerator)	$d$ (denominator)
$p \otimes \frac{p}{p}$	plain	plain	plain
$\ell \otimes \frac{p}{p}$	loose	plain	plain
$\ell \otimes \frac{p}{\ell}$	loose	plain	loose
$\ell \otimes \frac{\ell}{\ell}$	loose	loose	loose
$t \otimes \frac{p}{p}$	tight	plain	plain
$t \otimes \frac{p}{\ell}$	tight	plain	loose
$t \otimes \frac{\ell}{\ell}$	tight	loose	loose
$t \otimes \frac{p}{t}$	tight	plain	tight
$t \otimes \frac{\ell}{t}$	tight	loose	tight
$t \otimes \frac{t}{t}$	tight	tight	tight
trim	trim	trim	trim

**Table 3.** A summary of the different tagging strategies considered, including the notation, and the degree of grooming for the mass, and numerator and denominator of the shape observable. For simplicity, we have suppressed the jet radius,  $R$ . The definitions of plain, loose, tight and trim are given in the text.

The explicit numerators ( $n$ ) and denominators ( $d$ ) for the different observables are summarized in Tab. 2.

As our organizing principle for classes of jet substructure taggers, we use the type of grooming applied to the initial mass cut, and the type of grooming applied to the numerator and denominator of the two-prong observable. We use the notation

$$m \otimes \frac{n}{d} \tag{4.6}$$

to denote the grooming applied to a particular observable, where  $m$ ,  $n$ , and  $d$  can take the values

- plain ( $p$ ): no grooming applied;
- loose ( $\ell$ ): SoftDrop with  $z_{\text{cut}} = 0.05$ ,  $\beta = 2$ ;
- tight ( $t$ ): mMDT with  $z_{\text{cut}} = 0.1$ .

We also study trimmed jets,

- trim: trimming with  $R_{\text{sub}} = 0.2$ ,  $z_{\text{cut}} = 0.05$  and the  $k_T$  algorithm to perform the reclustering, as used by ATLAS.

In general, to have a good 2-prong tagging strategy, we want to have

$$m \geq d \geq n, \tag{4.7}$$

Parameter	Values Scanned
Jet Radius $R$	0.8
Jet Shape	$D_2, N_2, M_2, \tau_{21}$
Jet Shape Angular Exponent $\beta$	1, 2
Jet $p_T$	500 GeV, 1000 GeV, 2000 GeV

**Table 4.** Jet shapes and parameters scanned for each of the different strategies proposed in Tab. 3.

where  $\geq$  refers to the aggressiveness of the groomer, with  $t > \ell > p$ .

The complete set of configurations that we consider is given in Tab. 3. These constitute generic grooming strategies, and will be studied for each of  $N_2$ ,  $D_2$ , and  $\tau_{21}$ . They include the dichroic ratios, as well as the current ATLAS and CMS approaches as specific examples. This will allow us to draw general conclusions about the performance and robustness of jet substructure taggers.

While our general approach is based on studying the different classes of grooming strategies in Tab. 3, for each of these different classes of strategies we will also scan different parameters. In particular, we will scan the jet shape, jet shape angular exponent, and jet  $p_T$ . The values scanned are summarized in Tab. 4. This allows us to understand if the conclusions drawn are associated with specific observables within a given strategy, as well as to optimize over these parameters. Due to the large number of physics and detector parameters that are varied in our study, only a subset of plots will be presented in the paper. A summary of the observables scanned, highlighting those which we find to be most promising, will be given in Fig. 13.

## 5 Theory Robustness

In this section, we study robustness to hadronization and underlying event, which we categorize as “Theory” robustness. Robustness to the detector, and pile-up are treated in Sec. 6.

### 5.1 Hadronization

We begin by studying the robustness of different tagging techniques to hadronization. As discussed in Sec. 2, this must be interpreted with some care, since the unhadronized events are not themselves physical. Nevertheless, the comparison of hadronized and unhadronized distributions is the best proxy for understand the impact of hadronization short of performing an analytic calculation. To ensure that our conclusions are robust, ideally we would consider parton shower generators which implement different hadronization models. For example, the PYTHIA shower uses the string model [131, 132], while HERWIG++ uses the cluster model [133, 134]. See for example Refs. [135–137] for a more detailed discussion. Unfortunately, due to the restricted scope of this report, here we only consider PYTHIA. The effect of hadronization on two-prong substructure observables has been studied in [54, 63, 64, 88].

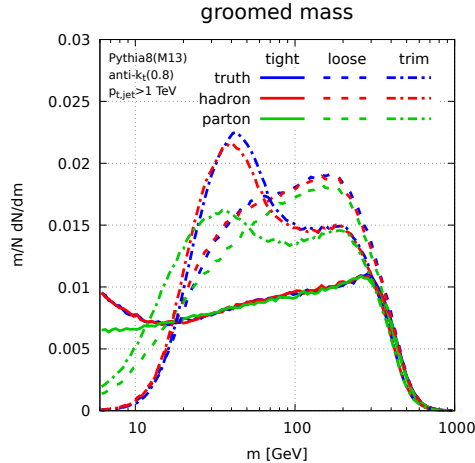


**Figure 5.** Mass distribution after grooming for the three groomers considered in this paper. The distributions are shown at parton level, at hadron level, and at truth level (i.e. including both hadronization and the underlying event).

Before studying robustness under hadronization vs. performance quantitatively, we will begin by showing several distributions with and without hadronization. This will help to introduce the different observables, as well as to give the reader a feeling for the robustness at the level of the shape of the distribution, and how this compares to our resilience measure.

In Fig. 5, we show the jet mass distribution for the three grooming strategies considered in this paper, for parton, hadron, and truth levels. Although we will not focus directly on the mass distribution in this paper, it plays an important role since all of our studies will be performed with jet mass cuts. Here we see two primary features. First, all three groomers give rise to significantly different mass distributions. This has been discussed in detail in Refs. [37, 85]. Second, with both tight and loose grooming, the distributions are robust to hadronization. This is particularly true for tight grooming where hadronization has almost no effect, except at extremely small values of the observable. On the other hand, the trimmed mass distribution is not robust to hadronization effects.

In Fig. 6, we show distributions for the observables that will be of primary interest in this study, namely  $D_2$ ,  $N_2$ , and a dichroic version of  $D_2$ , measured on both background and signal jets. In all cases, we see that hadronization has a sizable effect on the shape of the distribution, pushing it to larger values. For the  $D_2$  observable, hadronization is mostly isolated to small values of the observable, and at larger values reduces simply to a shift of the distribution. This has been discussed in detail for the case of  $D_2$  in Refs. [54, 63, 64]. For the  $N_2$  observable, hadronization effects are larger and are significant throughout the entire distribution. Indeed, when we study performance and robustness quantitatively, we will find that while  $N_2$  type observables tend to be more performant, they are also less resilient to hadronization effects.

Since the primary role of hadronization is to push the distributions to larger values

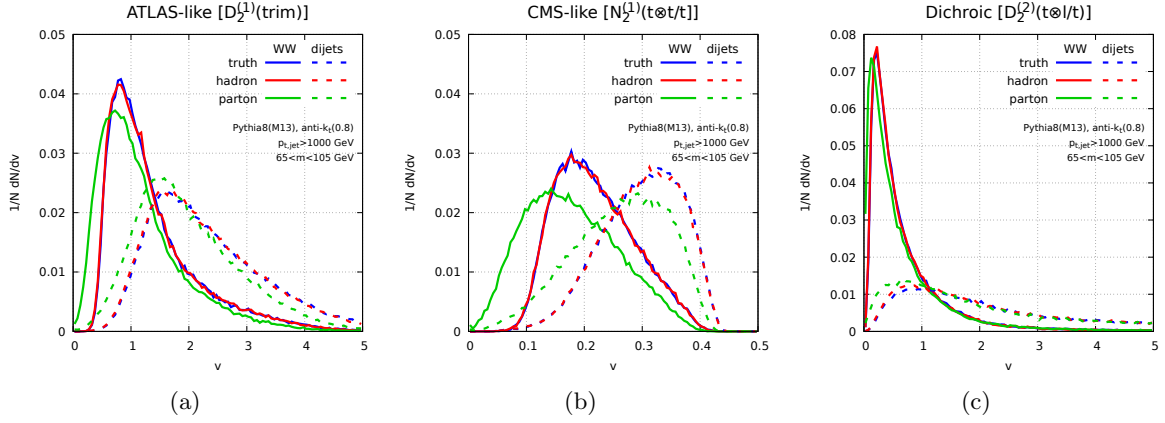


**Figure 6.** Distribution of three representative shapes:  $D_2^{(1)}$  computed on the trimmed jet (ATLAS-like),  $N_2^{(1)}$  computed on the tight (mMDT) jet (CMS-like), and the dichroic  $D_2^{(2)}$  with numerator computed on the loose jet and denominator computed on the tight jet (Dichroic). The distributions are shown at parton level, at hadron level, and at “truth” level (i.e. including both hadronization and the underlying event), for both  $WW$  (solid) and dijet (dashed) events.

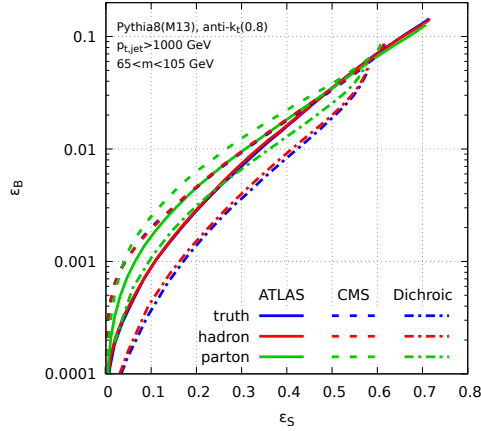


**Figure 7.** ROC curves corresponding to the shapes plotted on Fig. 6. The three line types correspond to the three possible shape choices.

at small values of the observable, the performance of the observables is typically highly sensitive to hadronization, particularly at high signal purity. In Fig. 7 we illustrate this (lack of) robustness to hadronization at the level of the ROC curves for the different shape choices. In all cases, we see that hadronization considerably improves the performance of the observables. This is particularly true at high signal purity, and decreases as the signal purity is decreased. Since the region of high signal purity is typically that of interest for jet substructure studies, this emphasizes the importance of understanding the robustness of observables to hadronization effects.

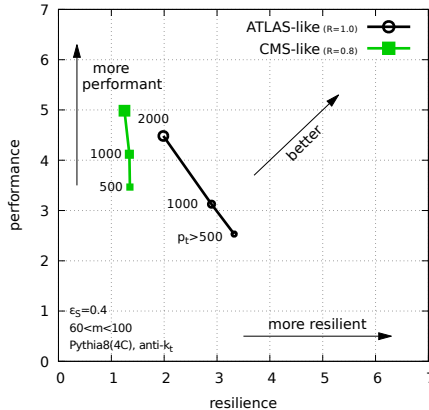


**Figure 8.** An illustration of the performance-resilience plane that will be used to illustrate our results. More performant observables lie to the top, more resilient observables to the right, and better observables in the upper-right corner.

Having given a feel for the modifications due to hadronization at the level of both distributions and ROC curves, we now use our performance and resilience measures to perform a quantitative study. Since our visualization method allows a considerable amount of information to be condensed into a single plot, we first briefly review our presentation method with a sample plot. In Fig. 8 we show a plot in the performance-resilience plane, in which we will display our results. More performant observables appear higher on the  $y$ -axis (towards the top), while more robust (resilient) observables appear higher on the  $x$ -axis (to the right), as indicated by the arrows. A performant and resilient observable will appear in the upper right corner. For each observable, we also perform a scan of  $p_T$ , from 500 – 2000 GeV, which are illustrated by the three connected points. This will be the default format in which we display our results throughout the rest of this paper.

In Figs. 9 and 10, we show the performance-resilience plots for the effects of hadronization for the different observables considered in this study. Fig. 9 shows  $D_2$ ,  $N_2$ , and dichroic  $D_2$  for the different grooming strategies, while in Fig. 10 we consider fixed grooming strategies in each plot, but different jet shape observables. We first notice that, in almost all cases, a dichroic form of the observable can be used to improve resilience while maintaining a similar level of performance. Among the shapes, we find that  $D_2$  tends to be the most robust, while  $N_2$  tends to be slightly more performant. This agrees with what was seen by studying the distributions in Fig. 6 by eye, however, we are now able to quantify this. We will see that this conclusion remains true under a larger scan of observables in Sec. 5.3. We also notice that for almost all the observables the trends with  $p_T$  are similar.

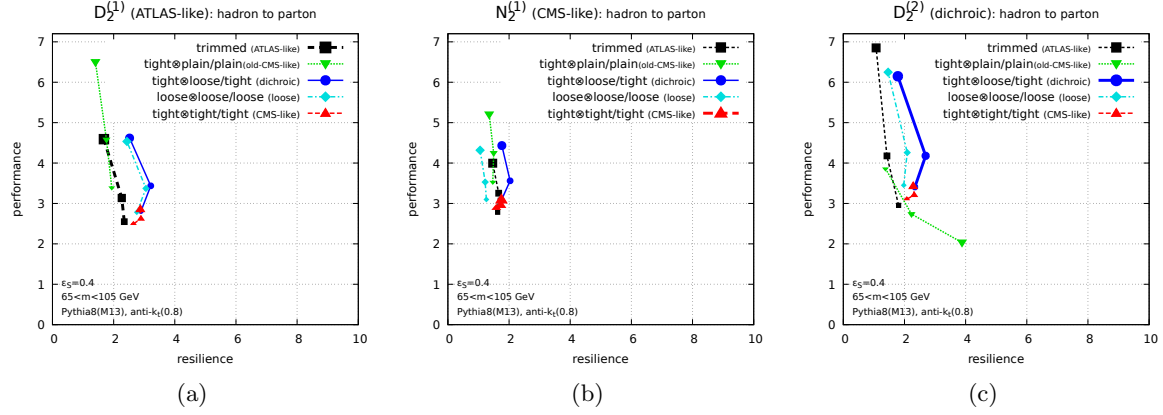


**Figure 9.** Plots of the performance-resilience plane under the addition of hadronization effects for the standard jet shape observables with different grooming strategies.

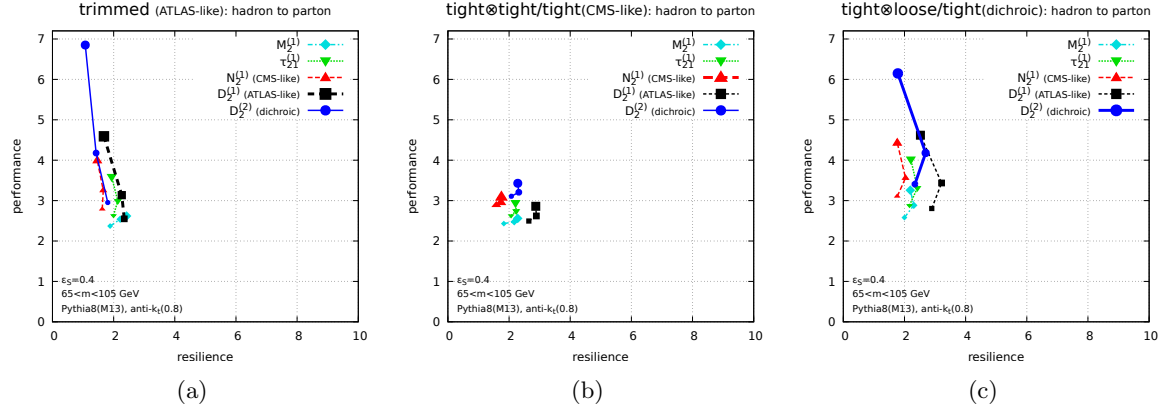


**Figure 10.** Plots of the performance-resilience plane under the addition of hadronization effects for different jet shape observables, with fixed grooming strategies.

## 5.2 Underlying Event

We can now repeat the same exercise performed for hadronization to study the robustness to underlying event. The results in the performance-resilience plane are shown in Figs. 11 and 12. These are identical to Figs. 9 and 10 but measure the robustness to underlying event instead of hadronization. The first thing that is clear from comparing Figs. 9 and 10 with Figs. 11 and 12 is that with modern grooming techniques, we are comparatively much less sensitive to underlying event than to hadronization effects. With the exception of the tight@plain/plain grooming strategy (which indeed does not groom the observable), all the standard observables with are robust to underlying event for all the different grooming strategies. Similarly, with the exception of the dichroic  $D_2$  observable, all the different jet shape observables in this study are also robust to underlying event. We believe that this should be viewed as a success

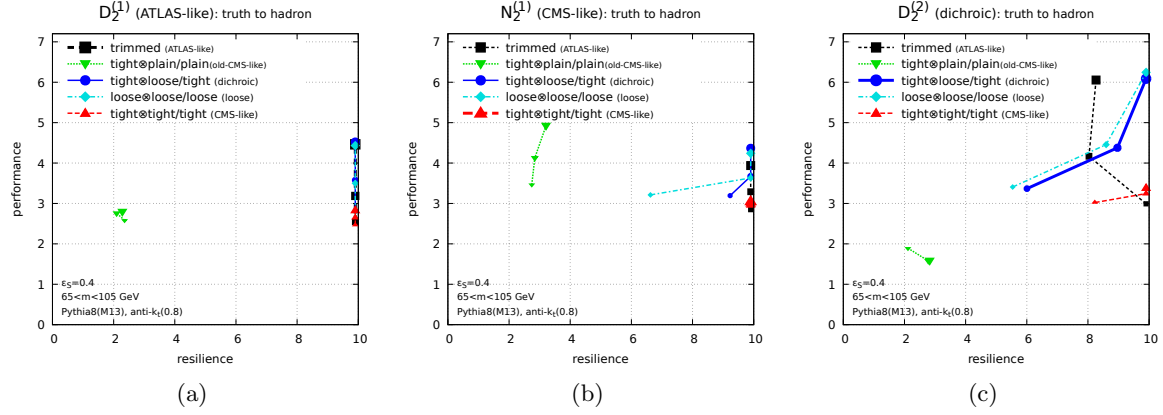


**Figure 11.** Plots of the performance-resilience plane going from hadron level to truth level (inclusion of underlying event) for the standard jet shape observables with different grooming strategies.

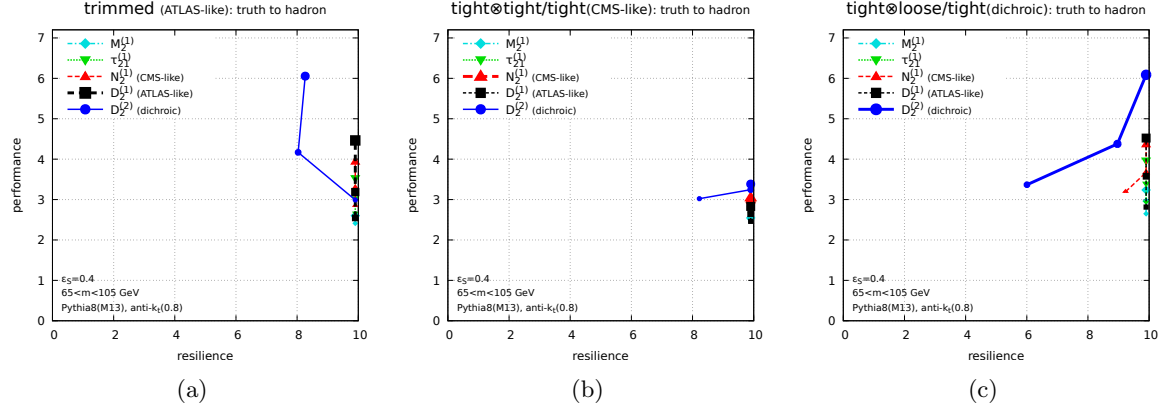


**Figure 12.** Plots of the performance-resilience plane going from hadron level to truth level (inclusion of underlying event) for different jet shape observables, with fixed grooming strategies.

of modern grooming tools. We also believe that it is desirable, since underlying event effects are much less under theoretical control than hadronization effects.

### 5.3 Towards Improved Performance and Robustness for ATLAS and CMS

The strategies used by ATLAS and CMS, namely trimmed  $D_2$  [54, 66] and SoftDropped  $N_2$  [81] with DDT [87] are specific examples of the broader approaches to two-prong tagging discussed above, and therefore our study allows us to gain insight into the different tagging strategies used by the collaborations,<sup>2</sup> as well as to suggest improved observables.

<sup>2</sup>And perhaps even into the sociology of the different experiments! However, such conclusions should be taken with a grain of salt.



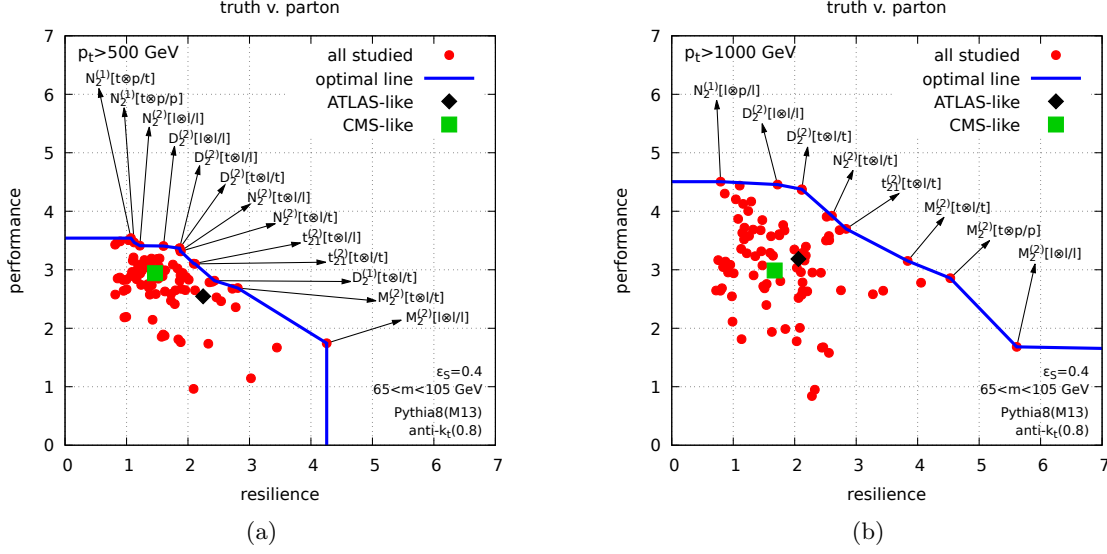


**Figure 13.** The performance-resilience plane for the different observables scanned in our study at (a) 500 GeV and (b) 1000 GeV. The ATLAS- and CMS-like observables are marked in black and green, respectively. In both cases, more robust, and more performant observables can be selected, and a number of such observables are marked.

An overall scan of all the observables used in this study in the performance-resilience plane is shown in Fig. 13. The current CMS and ATLAS observables are highlighted with the black and green markers, respectively. We can draw two interesting conclusions from this plot. First, for  $p_T > 500$  GeV, it appears as though ATLAS is using a more robust, but less performant observable, while CMS is using a more performant, but less robust observable. This must be caveated by the fact that we have not performed a full detector study, though it is suggestive. Second, we can choose from the observables considered in our study observables that are simultaneously more performant, and more resilient than those that are currently being used. At 500 GeV the gains in performance are fairly minimal, but at 1000 GeV, it seems that there are considerable gains in performance and robustness to be made. The names of a large variety of those observables which lie on the upper boundary of the performance-resilience space are marked in the figure.

Looking more closely at the observables along this upper boundary, we see that there is in fact considerable structure, and a number of general lessons can be learned. First, as we move along this boundary from least resilient to most resilient, we transition from  $N_2$  observables which are the most performant, but less robust, through  $D_2$ , to  $M_2$ , which is more robust, but less performant. This was also clearly observed in the distributions of Fig. 6. We believe that this is due to the fact that  $N_2$  has a hard phase space boundary, and therefore non-perturbative effects are not isolated at small values of the observable, although it would be

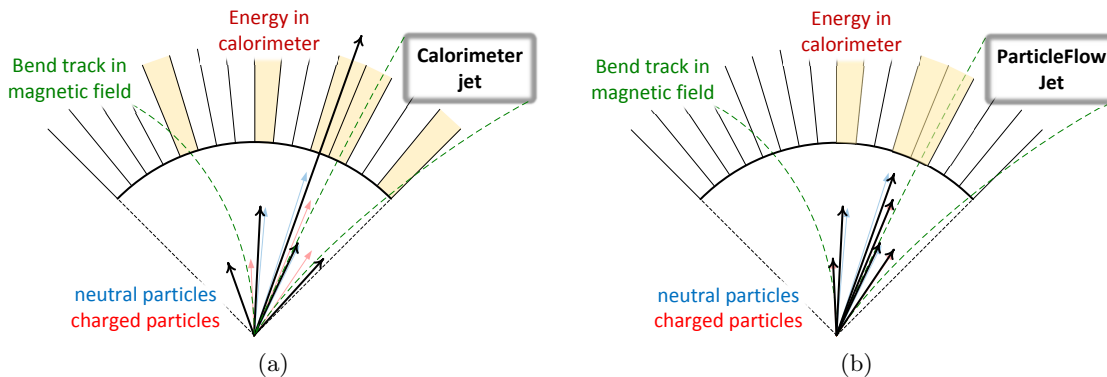


**Figure 14.** An illustration of the basic jet features for the configuration A (ATLAS-like, calorimeter only) and configuration C (CMS-like, particle flow using tracks and calorimeter) detector signal models. The solid black arrows indicate the jet composition from representations of neutral (pale blue) and charged (pale red) particles by calorimeter towers or reconstructed tracks. The green dashed curves show charged particle tracks bend in the magnetic field. Both illustrations show the same truth-level jet.

interesting to understand this behavior in more detail.

A second pattern that is observed is that in almost all cases dichroic variants of the observables of the form  $t \otimes \frac{p}{t}$  or  $t \otimes \frac{\ell}{t}$  exhibit improved performance without significant loss in resilience. We believe that it is worthwhile for the experiments to consider some of the dichroic observables that were newly introduced in Sec. 4.2 with simultaneous performance and resilience in mind. We have highlighted in Fig. 13 that a whole interesting phase space of such observables exist, which map out the performance-resilience plane. Different observables could be chosen depending on the particular needs of a given study.

## 6 Experimental Robustness

Having discussed robustness to theoretical issues, we now continue through our chain of realism of Fig. 1 and consider robustness to detector effects. In Sec. 6.1 we describe our detector model. In Sec. 6.2 we describe pile-up removal. In Sec. 6.3 we study the robustness of jet mass to detector effects. A more comprehensive study is left to a dedicated publication.

### 6.1 Detector Models

The detector response is modeled by subjecting the particle-level objects<sup>3</sup> to a simple acceptance and smearing model representing tracking detectors as well as calorimeters. Basic detector feature descriptors are considered together with response features and signal reconstruction strategies similar to the ATLAS and CMS experiments at the LHC. The respective

<sup>3</sup>Those are stable particles produced by the generator that potentially reach a detector. This principally requires a particle lifetime  $\tau$  in the laboratory frame given by  $c\tau > 10$  mm.

Signal	Model parameters			
	Coverage	$p_T^{\min}$	$p_T^{\max}$	Resolution function parameters
<b>Configuration A</b> ( $R_{\text{calo}} = 1150$ mm, $B_{\text{solenoid}} = 2$ T)				
Towers (EM)	$ \eta  < 2.5$	500 MeV	10 TeV	$a_{\text{calo}} = 10\% \times \sqrt{\text{GeV}}$ $b_{\text{calo}} = 0$ $c_{\text{calo}} = 0.7\%$
Towers (HAD)	$ \eta  < 4.9$	500 MeV	10 TeV	$a_{\text{calo}} = 50\% \times \sqrt{\text{GeV}}$ $b_{\text{calo}} = 0$ $c_{\text{calo}} = 3\%$
<b>Configuration C</b> ( $R_{\text{calo}} = 1290$ mm, $B_{\text{solenoid}} = 4$ T)				
Towers (EM)	$ \eta  < 2.5$	500 MeV	10 TeV	$a_{\text{calo}} = 3\% \times \sqrt{\text{GeV}}$ $b_{\text{calo}} = 0$ $c_{\text{calo}} = 0.5\%$
Towers (HAD)	$ \eta  < 4.9$	500 MeV	10 TeV	$a_{\text{calo}} = 100\% \times \sqrt{\text{GeV}}$ $b_{\text{calo}} = 0$ $c_{\text{calo}} = 5\%$
Tracks	$ \eta  < 2.5$	1 GeV	300 GeV	$a_{\text{track}} = 0.015\% \times \text{GeV}^{-1}$ $c_{\text{track}} = 0.5\%$

**Table 5.** Principal properties and smearing parameters of the detector model configurations A and C. Electromagnetic (EM) towers have a tower size of  $\Delta\eta \times \Delta\phi = 0.025 \times 0.025$ , while hadronic (HAD) towers have  $\Delta\eta \times \Delta\phi = 0.1 \times 0.1$ . Tracks are not modeled in configuration A, while configuration C models both tracks and calorimeter signals to simulate the effect of a particle flow algorithm. The resolution function parameters  $a_{\text{calo}}$ ,  $b_{\text{calo}}$ , and  $c_{\text{calo}}$  are used together with the resolution function in Eq. 6.1 to determine the width of the Gaussian energy smearing. Similarly,  $a_{\text{track}}$  and  $c_{\text{track}}$  are used in Eq. 6.2 to determine the width of the track- $p_T$  resolution smearing.

model configurations are A (ATLAS-like [138]) and C (CMS-like [139]). Effects from particles showering in calorimeters are not modeled.

Both configurations feature cylindrical detectors around the collision vertex with full azimuthal coverage  $-\pi < \phi < \pi$ . The detector modeling produces a final state represented by a list of *pseudoparticles* which are proxies for detector signals generated by stable particles. Particles emitted at pseudorapidities  $|\eta| > 4.9$  and non-detectable particles like neutrinos are excluded from this modeling and thus not part of this final state.

In configuration A, the pseudoparticles are produced by a calorimeter-only detector model with regular projective readout in  $(\eta, \phi)$  space. The energy of all stable particles generating hadronic shower when interacting with the detector material is collected in hadronic (HAD)

*calorimeter towers* of size  $\Delta\eta \times \Delta\phi = 0.1 \times 0.1$ . Electrons, positrons, and photons emitted within  $|\eta| < 2.5$  fill electromagnetic (EM) towers of size  $\Delta\eta \times \Delta\phi = 0.025 \times 0.025$  with their energy, mimicking the typical coverage of the high granularity electromagnetic calorimeter. The direction of neutral particles is the generated direction at the vertex, while for all charged particles  $\phi$  is changed to the azimuth at the entry point of the particle into the calorimeter. This entry point is calculated using the particle trajectory in an axial uniform magnetic field of  $B_{\text{solenoid}} = 2\text{T}$  and the radius  $R_{\text{calo}} = 1150\text{ mm}$  of on the calorimeter front face. If the transverse momentum of the charged particle is too low to reach the calorimeter, i.e. its trajectory in the magnetic field does not exceed  $R_{\text{calo}}$ , the particle is considered invisible for the detector and thus ignored for further analysis. For particles reaching the calorimeter, the (bent) trajectory is not radial anymore at the front face. This suggests a distribution of the particle energy into more than one tower. In this model there is no energy sharing between towers, as this would require to at least model the longitudinal energy distribution in an electromagnetic or hadronic shower, with considerable computational effort.

After all energy is collected, the finite calorimeter resolution is modeled by smearing the tower energy  $E_{\text{tower}}$  following a Gaussian distribution with width  $\sigma_{E_{\text{tower}}}$  given by the canonical calorimeter resolution function:

$$\frac{\sigma_{E_{\text{tower}}}(E_{\text{tower}})}{E_{\text{tower}}} = \sqrt{\frac{a_{\text{calo}}^2}{E_{\text{tower}}} + \frac{b_{\text{calo}}^2}{E_{\text{tower}}^2} + c_{\text{calo}}^2}. \quad (6.1)$$

The three components of this function are the stochastic term  $a_{\text{calo}}$  reflecting sampling and intrinsic shower fluctuations, the noise term  $b_{\text{calo}}$  quantifying the detector noise, and the constant term  $c_{\text{calo}}$  capturing fluctuations introduced in the process of the detector signal extraction. The values for  $a_{\text{calo}}$  and  $c_{\text{calo}}$  are shown in Table 5. The detector noise is not modeled, thus the noise term is  $b_{\text{calo}} = 0$  for both configurations.

The tower energy after smearing is required to pass  $p_{\text{T}}^{\text{tower}} > p_{\text{T}}^{\text{min}}$ . Towers passing this requirement are converted into massless pseudoparticles using the nominal tower center  $(\eta_{\text{tower}}, \phi_{\text{tower}})$  and the tower energy  $E_{\text{tower}}$  ( $(E_{\text{tower}}, \eta_{\text{tower}}, \phi_{\text{tower}}) \mapsto (E_{\text{tower}}, \vec{p}_{\text{tower}})$  with  $|\vec{p}_{\text{tower}}| = E_{\text{tower}}$ ).

Configuration C models a particle flow signal from a tracking detector combined with a calorimeter. Charged particles are bent in an axial uniform magnetic field with  $B_{\text{solenoid}} = 4\text{ T}$ . The transverse momentum of the charged particles emitted within a tracking detector acceptance of  $|\eta| < 2.5$  is smeared along a Gaussian distribution function with width  $\sigma_{p_{\text{T}}^{\text{track}}}$  given by:

$$\frac{\sigma_{p_{\text{T}}^{\text{track}}}}{p_{\text{T}}^{\text{track}}} = \sqrt{(a_{\text{track}} \cdot p_{\text{T}}^{\text{track}})^2 + c_{\text{track}}^2}. \quad (6.2)$$

If  $p_{\text{T}}^{\text{track}}$  after smearing is within  $p_{\text{T}}^{\text{min}} < p_{\text{T}}^{\text{track}} < p_{\text{T}}^{\text{max}}$ , the charged particle is added to the list of pseudoparticles with its direction at the interaction vertex. The trajectories of all charged particles within  $|\eta| < 2.5$  and outside of this transverse momentum range, and all charged particles with  $|\eta| > 2.5$ , are extrapolated to the front face of the calorimeter at  $R_{\text{calo}} = 1290$

mm. If the extrapolated particle trajectory reaches the calorimeter, the particle energy is added to a calorimeter tower at the extrapolated  $\phi$ , similar to the treatment of all charged particles in configuration A.

The energy of neutral particles is added to the calorimeter tower in the same way as in configuration A. The selection employing  $p_T^{\text{tower}} > p_T^{\text{min}}$  is applied as well after the tower energy smearing with the parameters for configuration C given in Table 5. Figure 14 shows the calorimeter-only composition of a given truth-level jet in configuration A together with the track-and-calorimeter jet composition of configuration C. The two model configurations produce significantly different jet compositions, in particular with respect to the energy flow from low- $p_T$  constituents.

## 6.2 Pile-Up Removal

Due to the high pile-up environment of the LHC, pile-up mitigation techniques [140–146] are also widely used, which eliminate soft radiation from the event. Since this radiation is uncorrelated with the underlying hard scattering, this can in principle be done, and a variety of techniques exist. In this paper we use Area Subtraction [140, 147] and SoftKiller [145] as representative of these techniques.

In the SoftKiller approach, the event is broken into patches, and we define

$$\rho = \text{median} \left\{ \frac{p_{Ti}}{A_i} \right\}. \quad (6.3)$$

SoftKiller then removes particles below a cutoff  $p_T^{\text{cut}}$ , chosen such that  $\rho = 0$ . We have

$$p_T^{\text{cut}} = \text{median}\{p_{Ti}^{\text{max}}\}. \quad (6.4)$$

SoftKiller has been shown to provide good performance for removing pile-up contamination.

**(A few points (I'll try to come back to this part later): (i) maybe the 1st equation could go into the area–median description, (ii) do we want to give all the details of the area–median parameters we've used (I'd say yes), (iii) we should mention that SK is fast, (ic) wqe should add a reference to PUPPI as an alternative used by CMS. –gs)**

PUPPI: [146]

## 6.3 Impact on Mass Resolution

We now perform a study of the impact of detector and pile-up effects on mass resolution. This will highlight the need to perform a more sophisticated study when considering detector effects, which will be left to a future publication.

In Fig. 15, we show distributions of the groomed mass for a hadronically decaying boosted  $W$  boson in our CMS-like and ATLAS-like detectors at different values of the jet  $p_T$ . We see that the detector has a significant impact on the distributions, particularly as the  $p_T$  is increased. We also see that both detectors have a similar performance, despite their different approaches. Despite the fact that CMS has particle flow, at high  $p_T$  there is a trade

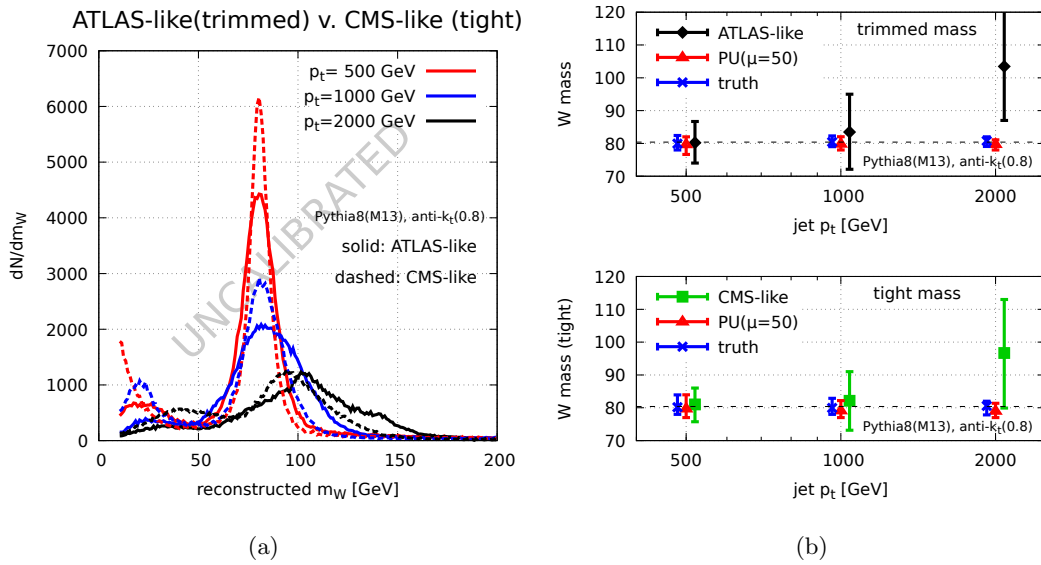


**Figure 15.** Mass reconstruction with detector effects as a function of the jet  $p_T$ .

off between tracking and calorimetry, which is better in ATLAS, leading to comparable detector resolution. Furthermore, in the full experiments, the reconstruction algorithms are complementary and adapted to the experiments' detector technologies to achieve similar performance. Due to the fact that the end results of the two detectors are quite similar, we find it unwise to draw any deeper conclusions, since there are potentially other effects, not included in our simulation, that could determine the final result.

This short study highlights the essential importance of understanding detector effects when designing jet substructure observables. Although we have found that the  $N_2$  and  $D_2$  observables emphasize, respectively, performance and robustness, it would also be interesting to understand if the different detectors played a role in the choice of one observable as compared with the other. As highlighted by the specific example of the groomed jet mass in this section, such a study requires considerable care to perform in a meaningful manner. The detectors have a large impact, and the two detectors appear qualitatively similar in our analysis setup. Differences may therefore be due to more subtle features, beyond those included in our study, and this is probably something that is best left to the experimental collaborations to study with realistic detector simulations. We hope that this study motivates the experimental collaborations to further investigate the performance and robustness of different two-prong tagging observables at each of the different steps along the chain of realism in order to understand the different choices in observables.

## 7 Polarization Dependence

The focus of this paper is on the robustness of jet substructure observables for two-prong tagging. As has been discussed, for background QCD jets one is interested in robustness to additional QCD contamination and detector effects. For signal jets, there is another consideration, namely the specific nature of the decaying electroweak-scale resonance, which can also affect the substructure observables. Assuming that this electroweak-scale particle is a color-singlet decaying to quarks, it is completely characterized by its spin structure.

All of our taggers consist of two conceptually distinct components, which will be affected in different ways by the polarization. We begin by making a cut on the (groomed) mass, followed by a cut on a particular jet shape which is sensitive to the two-prong structure. These two steps are associated with very different physics. A jet from a  $W \rightarrow q\bar{q}$  decay consists of two collimated sprays of radiation, which are proxies for the  $q$  and  $\bar{q}$ , along with radiation emitted from the dipole. Ideally, a groomer should terminate when it de-clusters the jet into two subjets corresponding to the jets initiated by the two quarks. If there is a large fraction of decays where the momentum sharing between the two subjets is hierarchical, though, then the groomer can remove one of the subjets. In this case, the jet will fail the groomed mass criteria. Since the polarization controls the momentum sharing of the subjets, this introduces a sensitivity on the polarization into the tagging procedure. On the other hand, the 2-prong tagging observables that we consider are all formed as ratios of an observable which is sensitive to radiation from the prongs, divided by a mass-type observable, which (largely) removes the dependence on the momentum sharing of the subjets.

In this section, we consider two main issues, namely the dependence of the standard jet substructure observables to the polarization of the signals, and the ability to perform polarimetry using jet substructure observables measured on the hadronic decay products.

### 7.1 Performance Impact of Polarization

We begin by studying the sensitivity of two-prong taggers to polarization. To do this, we consider samples of hadronically decaying  $W$ s, which are either purely transversely polarized, purely longitudinally polarized, or have the Standard Model fraction (mostly transverse). The details of the sample generation were discussed in Sec. 3.3.

In Fig. 16a, we show the  $D_2$  observable as measured on longitudinal and transverse hadronically decaying  $W$  bosons, as well as the Standard Model mixture, as a representative example of the dependence of a two-prong tagger on polarization. From this figure, we see that the jet shape observable itself is remarkably insensitive to the polarization, due to its ratio nature. However, it is important to emphasize that this does not imply that the tagging performance is also independent of the polarization. As can be seen in Fig. 16b, the tagging performance is significantly worse for transversely polarized  $W$  bosons as compared with longitudinally polarized  $W$  bosons. This is due to the fact that transversely polarized  $W$  bosons have a more asymmetric energy sharing, and it is therefore more likely that one of the subjet prongs is groomed away, leading to the jet failing the mass cut. This difference between

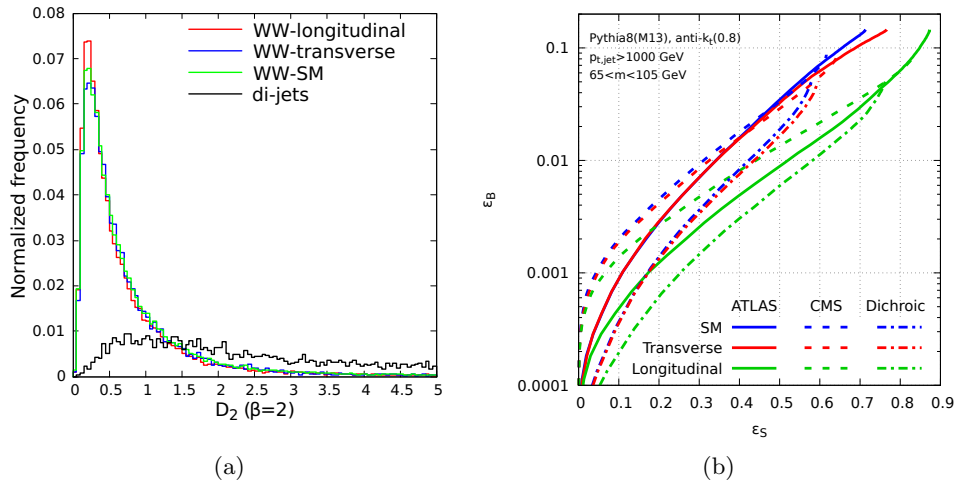


**Figure 16.** a) Distributions of the  $D_2$  observable as measured on the samples with different polarization compositions. These observables are found to be largely insensitive to the polarization. b) ROC curves comparing the different grooming strategies for different polarization samples. While the polarization has a limited effect on the jet shape observables, it modifies the groomed mass acceptance, and therefore the tagging efficiency, significantly.

longitudinally and transversely polarized bosons should be taken into account in studies at the LHC. It would also be interesting to develop tagging or reconstruction schemes that are less sensitive to polarization.

## 7.2 Tagging Longitudinal vs. Transverse Bosons

Having understood the dependence of standard jet substructure observables on polarization, it is interesting to know whether jet substructure observables are able to tag distinct polarizations on hadronically-decaying particles, and with what efficiency this can be done. Since the standard two-prong tagging observables are not particularly sensitive to the polarization, a different observable must be used to tag polarizations. Here, we do not perform a comprehensive study, but restrict ourselves to studying a particular example of an observable which is sensitive to the  $W$  polarization, and we evaluate its performance for distinguishing transverse and longitudinal  $W$  bosons.

The sole impact of the polarization of the decaying object is to determine the kinematics of the decaying subjets. Indeed, this can be made rigorous in the sense of a factorization theorem for boosted jets in the two-prong limit. We are therefore interested in an observable that is sensitive to the kinematics of the two subjets. While a variety of different observables could be considered, here we consider the  $z_g$  observable [85, 126, 148], which measures the momentum sharing of the subjets. The precise definition of  $z_g$  was given in Sec. 3.2, which



we recall for convenience

$$z_g = \frac{\min[p_{Ti}, p_{Tj}]}{p_{Ti} + p_{Tj}}. \quad (7.1)$$

Here  $p_{Ti}$  and  $p_{Tj}$  are the momenta of the first set of subjets that pass the SoftDrop criteria.

Since we are focused on robustness in this paper, it is also worth commenting on the robustness of the  $z_g$  observable. For signal jets, since this observable measures global energy properties of the subjets, it is stable. Interestingly, it is also remarkably stable on the background, where it flows in the high  $p_T$  limit to the QCD splitting function [85, 126, 148].

In Fig. 17a, we show the  $z_g$  distribution for different polarized  $W$  bosons. For reference, the  $z_g$  distribution for QCD dijets is also shown. The  $z_g$  distribution for transversely polarized  $W$  bosons follows most closely the QCD distribution, as expected, being peaked at small values of  $z_g$ . On the other hand, for longitudinally polarized  $W$  bosons, the  $z_g$  distribution is peaked at high values of  $z_g$ . This illustrates that the  $z_g$  observable is indeed behaving as expected, and is achieving sensitivity to the polarization of the decaying  $W$  boson only from its hadronic decay products. In Fig. 17b, we show the ROC curve for separating longitudinal from transverse  $W$  bosons. Here we see that  $z_g$  provides moderate separation power for tagging the polarization of the decaying  $W$  bosons. It would be interesting to investigate this further to see if more ideal observables could be found, however, we are not optimistic that significant improvement can be achieved, since the primary imprint of the polarization should be in the kinematics of the subjets.

## 8 Summary and Recommendations

In this paper, we performed a comprehensive study of performance and robustness for two-prong tagging, and provided a unifying approach to understanding different classes of two-prong taggers based on dichroic observables, which allow for different amounts of grooming in the numerator and denominator of observables. We introduced measures of robustness, in addition to the standard measures of performance, and we used these measures to study the robustness of two-prong taggers to theory issues, namely hadronization and underlying event. We believe that these will be of more general utility in jet substructure, and could be applied also to study three-prong tagging, for example.

As a part of our study, we have also introduced a number of new dichroic observables, which generalize the dichroic  $N$ -subjettiness observables to observables formed from the energy correlation functions. This offers a general and unifying approach to designing new jet substructure observables which are simultaneously performant and resilient. We have shown that the  $N_2$ -style observables used by CMS tend to be more performant, but less resilient than the  $D_2$ -style observables used by ATLAS. For a given observable, we have found that moving to a dichroic variant can typically improve performance without significantly decreasing its robustness to hadronization.

We have also studied the effect of polarization on two-prong taggers. We found that while polarization has minimal effect on standard two-prong tagging observables, since they

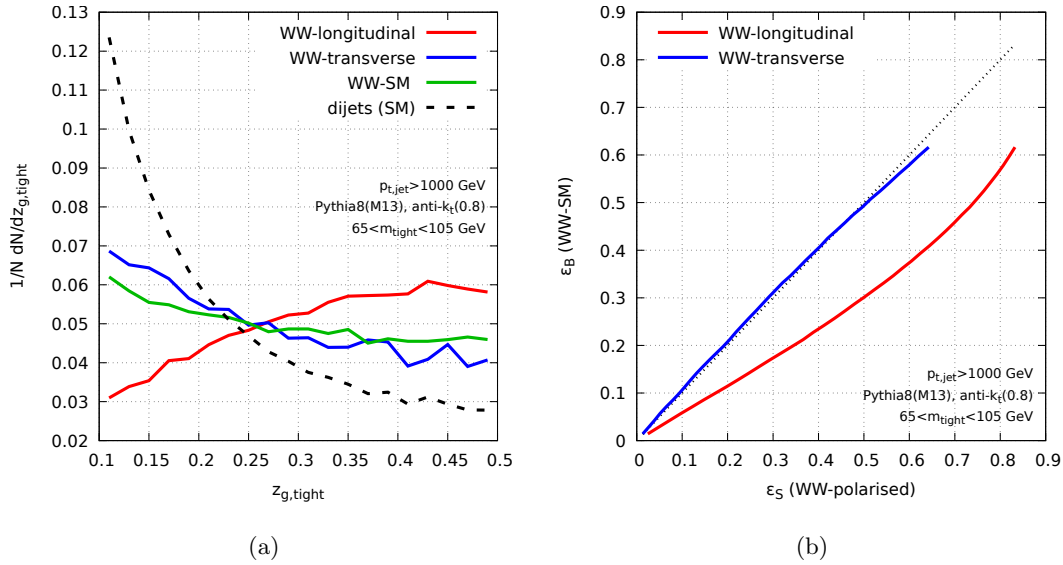


**Figure 17.** a) The  $z_g$  distribution as measured on boosted  $W$  samples with different polarization compositions. Transversely polarized  $W$ s behave similarly to the QCD background, while decent separation is observed between longitudinally polarized  $W$ s and transversely polarized  $W$ s. b) A ROC curve showing the separation between transversely- and longitudinally-polarized  $W$  bosons using the  $z_g$  observable. Moderate separation is observed.

are typically defined as ratios, it has a large effect on their tagging efficiency due to applied mass cuts. Significantly better tagging performance is observed for longitudinally polarized bosons. An interesting avenue beyond standard two-prong tagging is using jet substructure observables to tag the polarization of decaying Standard Model bosons using their hadronic decay products. We proposed the observable  $z_g$ , which measures the momentum sharing asymmetry between subjets, as an effective polarization tagger. We illustrated that separation between longitudinal and transverse bosons can be achieved. It would be interesting to study this problem in more detail.

We have identified a number of new two-prong taggers that outperform, in both robustness and tagging performance, those currently used by the ATLAS and CMS collaborations. These findings are summarized in Fig. 13, which also lists a number of promising new observables. We therefore believe that further studies using more detailed simulations of the ATLAS and CMS detectors, and ultimately on real data, would be of significant interest. More generally, we believe that the emphasis on a simultaneous evaluation of the performance and robustness, as well as the particular metrics introduced in this paper, will play a significant role in future studies of jet substructure techniques at the LHC.

## Acknowledgments

We thank the participants of Les Houches 2017 for a lively environment and useful discussions. The work of GS is supported in part by the Paris-Saclay IDEX under the IDEOPTIMALJE grant, by the French Agence Nationale de la Recherche, under grant ANR-15-CE31-0016, and by the ERC Advanced Grant Higgs@LHC (No. 321133). The work of JT is supported by the DOE under grant contract numbers DE-SC-00012567 and DE-SC-00015476. The work of IM is supported by Office of High Energy Physics of the U.S. Department of Energy under Contract No. DE-AC02-05CH11231, and the LDRD Program of LBNL.

## References

- [1] **CMS** Collaboration, S. Chatrchyan et al., *Search for a Higgs boson in the decay channel  $H$  to  $ZZ(^*)$  to  $q \bar{q} \ell^+ \ell^-$  in  $pp$  collisions at  $\sqrt{s} = 7$  TeV*, *JHEP* **1204** (2012) 036, [[arXiv:1202.1416](#)].
- [2] **CMS** Collaboration, *Search for a Standard Model-like Higgs boson decaying into  $WW$  to  $l \nu \bar{q} q$  in  $pp$  collisions at  $\sqrt{s} = 8$  TeV*, Tech. Rep. CMS-PAS-HIG-13-008, 2013.
- [3] **ATLAS** Collaboration, G. Aad et al., *Measurement of jet charge in dijet events from  $\sqrt{s} = 8$  TeV  $pp$  collisions with the ATLAS detector*, *Phys. Rev.* **D93** (2016), no. 5 052003, [[arXiv:1509.05190](#)].
- [4] **ATLAS** Collaboration, G. Aad et al., *Measurement of colour flow with the jet pull angle in  $t\bar{t}$  events using the ATLAS detector at  $\sqrt{s} = 8$  TeV*, *Phys. Lett.* **B750** (2015) 475–493, [[arXiv:1506.05629](#)].
- [5] *Performance of jet substructure techniques in early  $\sqrt{s} = 13$  TeV  $pp$  collisions with the ATLAS detector*, Tech. Rep. ATLAS-CONF-2015-035, CERN, Geneva, Aug, 2015.
- [6] **ATLAS** Collaboration, G. Aad et al., *Identification of boosted, hadronically decaying  $W$  bosons and comparisons with ATLAS data taken at  $\sqrt{s} = 8$  TeV*, *Eur. Phys. J.* **C76** (2016), no. 3 154, [[arXiv:1510.05821](#)].
- [7] **ATLAS** Collaboration, G. Aad et al., *Measurement of the differential cross-section of highly boosted top quarks as a function of their transverse momentum in  $\sqrt{s} = 8$  TeV proton-proton collisions using the ATLAS detector*, *Phys. Rev.* **D93** (2016), no. 3 032009, [[arXiv:1510.03818](#)].
- [8] *Studies of  $b$ -tagging performance and jet substructure in a high  $p_T$   $g \rightarrow b\bar{b}$  rich sample of large- $R$  jets from  $pp$  collisions at  $\sqrt{s} = 8$  TeV with the ATLAS detector*, Tech. Rep. ATLAS-CONF-2016-002, CERN, Geneva, Feb, 2016.
- [9] **ATLAS Collaboration** Collaboration, *Boosted Higgs ( $\rightarrow b\bar{b}$ ) Boson Identification with the ATLAS Detector at  $\sqrt{s} = 13$  TeV*, Tech. Rep. ATLAS-CONF-2016-039, CERN, Geneva, Aug, 2016.
- [10] **ATLAS Collaboration** Collaboration, *Discrimination of Light Quark and Gluon Jets in  $pp$  collisions at  $\sqrt{s} = 8$  TeV with the ATLAS Detector*, Tech. Rep. ATLAS-CONF-2016-034, CERN, Geneva, Jul, 2016.

- [11] **CMS Collaboration** Collaboration, *Measurement of the  $t\bar{t}$  production cross section at 13 TeV in the all-jets final state*, Tech. Rep. CMS-PAS-TOP-16-013, CERN, Geneva, 2016.
- [12] **CMS Collaboration** Collaboration, *Search for  $t\bar{t}H$  production in the  $H \rightarrow b\bar{b}$  decay channel with  $\sqrt{s} = 13$  TeV  $pp$  collisions at the CMS experiment*, Tech. Rep. CMS-PAS-HIG-16-004, CERN, Geneva, 2016.
- [13] **CMS Collaboration**, *Search for BSM  $t\bar{t}b\bar{b}$  Production in the Boosted All-Hadronic Final State*, Tech. Rep. CMS-PAS-EXO-11-006, 2011.
- [14] **ATLAS, CMS Collaboration**, S. Fleischmann, *Boosted top quark techniques and searches for  $t\bar{t}$  resonances at the LHC*, *J.Phys.Conf.Ser.* **452** (2013), no. 1 012034.
- [15] **ATLAS, CMS Collaboration**, J. Pilot, *Boosted Top Quarks, Top Pair Resonances, and Top Partner Searches at the LHC*, *EPJ Web Conf.* **60** (2013) 09003.
- [16] **ATLAS Collaboration**, *Performance of boosted top quark identification in 2012 ATLAS data*, Tech. Rep. ATLAS-CONF-2013-084, ATLAS-COM-CONF-2013-074, 2013.
- [17] **CMS Collaboration**, S. Chatrchyan et al., *Search for Anomalous  $t\bar{t}$  Production in the Highly-Boosted All-Hadronic Final State*, *JHEP* **1209** (2012) 029, [[arXiv:1204.2488](#)].
- [18] **CMS Collaboration** Collaboration, *Search for pair-produced vector-like quarks of charge  $-1/3$  decaying to  $bH$  using boosted Higgs jet-tagging in  $pp$  collisions at  $\sqrt{s} = 8$  TeV*, Tech. Rep. CMS-PAS-B2G-14-001, CERN, Geneva, 2014.
- [19] **CMS Collaboration** Collaboration, *Search for top-Higgs resonances in all-hadronic final states using jet substructure methods*, Tech. Rep. CMS-PAS-B2G-14-002, CERN, Geneva, 2014.
- [20] **CMS Collaboration**, V. Khachatryan et al., *Search for vector-like  $T$  quarks decaying to top quarks and Higgs bosons in the all-hadronic channel using jet substructure*, *JHEP* **06** (2015) 080, [[arXiv:1503.01952](#)].
- [21] **CMS Collaboration**, V. Khachatryan et al., *Search for a massive resonance decaying into a Higgs boson and a  $W$  or  $Z$  boson in hadronic final states in proton-proton collisions at  $\sqrt{s} = 8$  TeV*, *JHEP* **02** (2016) 145, [[arXiv:1506.01443](#)].
- [22] **ATLAS Collaboration**, G. Aad et al., *Search for high-mass diboson resonances with boson-tagged jets in proton-proton collisions at  $\sqrt{s} = 8$  TeV with the ATLAS detector*, *JHEP* **12** (2015) 055, [[arXiv:1506.00962](#)].
- [23] **ATLAS Collaboration**, M. Aaboud et al., *Searches for heavy diboson resonances in  $pp$  collisions at  $\sqrt{s} = 13$  TeV with the ATLAS detector*, [arXiv:1606.04833](#).
- [24] **ATLAS Collaboration**, M. Aaboud et al., *Search for heavy resonances decaying to a  $Z$  boson and a photon in  $pp$  collisions at  $\sqrt{s} = 13$  TeV with the ATLAS detector*, [arXiv:1607.06363](#).
- [25] **ATLAS Collaboration**, M. Aaboud et al., *Search for dark matter produced in association with a hadronically decaying vector boson in  $pp$  collisions at  $\sqrt{s}=13$  TeV with the ATLAS detector*, [arXiv:1608.02372](#).
- [26] **ATLAS Collaboration** Collaboration, *Search for resonances with boson-tagged jets in 15.5  $fb^{-1}$  of  $pp$  collisions at  $\sqrt{s} = 13$  TeV collected with the ATLAS detector*, Tech. Rep. ATLAS-CONF-2016-055, CERN, Geneva, Aug, 2016.

- [27] *Search for diboson resonances in the  $llqq$  final state in  $pp$  collisions at  $\sqrt{s} = 13$  TeV with the ATLAS detector*, Tech. Rep. ATLAS-CONF-2015-071, CERN, Geneva, Dec, 2015.
- [28] *Search for diboson resonances in the  $\nu\nu qq$  final state in  $pp$  collisions at  $\sqrt{s} = 13$  TeV with the ATLAS detector*, Tech. Rep. ATLAS-CONF-2015-068, CERN, Geneva, Dec, 2015.
- [29] **CMS Collaboration** Collaboration, *Search for dark matter in final states with an energetic jet, or a hadronically decaying  $W$  or  $Z$  boson using  $12.9 \text{ fb}^{-1}$  of data at  $\sqrt{s} = 13$  TeV*, Tech. Rep. CMS-PAS-EXO-16-037, CERN, Geneva, 2016.
- [30] **CMS Collaboration** Collaboration, *Search for new physics in a boosted hadronic monotop final state using  $12.9 \text{ fb}^{-1}$  of  $\sqrt{s} = 13$  TeV data*, Tech. Rep. CMS-PAS-EXO-16-040, CERN, Geneva, 2016.
- [31] **CMS Collaboration**, V. Khachatryan et al., *Search for dark matter in proton-proton collisions at 8 TeV with missing transverse momentum and vector boson tagged jets*, Submitted to: *JHEP* (2016) [[arXiv:1607.05764](#)].
- [32] **CMS Collaboration** Collaboration, *Searches for invisible Higgs boson decays with the CMS detector.*, Tech. Rep. CMS-PAS-HIG-16-016, CERN, Geneva, 2016.
- [33] **CMS Collaboration** Collaboration, *Search for top quark-antiquark resonances in the all-hadronic final state at  $\sqrt{s}=13$  TeV*, Tech. Rep. CMS-PAS-B2G-15-003, CERN, Geneva, 2016.
- [34] **CMS Collaboration** Collaboration, *Search for dark matter in association with a boosted top quark in the all hadronic final state*, Tech. Rep. CMS-PAS-EXO-16-017, CERN, Geneva, 2016.
- [35] I. Feige, M. D. Schwartz, I. W. Stewart, and J. Thaler, *Precision Jet Substructure from Boosted Event Shapes*, *Phys.Rev.Lett.* **109** (2012) 092001, [[arXiv:1204.3898](#)].
- [36] M. Field, G. Gur-Ari, D. A. Kosower, L. Mannelli, and G. Perez, *Three-Prong Distribution of Massive Narrow QCD Jets*, *Phys.Rev.* **D87** (2013), no. 9 094013, [[arXiv:1212.2106](#)].
- [37] M. Dasgupta, A. Fregoso, S. Marzani, and G. P. Salam, *Towards an understanding of jet substructure*, *JHEP* **1309** (2013) 029, [[arXiv:1307.0007](#)].
- [38] M. Dasgupta, A. Fregoso, S. Marzani, and A. Powling, *Jet substructure with analytical methods*, *Eur.Phys.J.* **C73** (2013), no. 11 2623, [[arXiv:1307.0013](#)].
- [39] A. J. Larkoski, J. Thaler, and W. J. Waalewijn, *Gaining (Mutual) Information about Quark/Gluon Discrimination*, *JHEP* **1411** (2014) 129, [[arXiv:1408.3122](#)].
- [40] M. Dasgupta, A. Powling, and A. Siodmok, *On jet substructure methods for signal jets*, *JHEP* **08** (2015) 079, [[arXiv:1503.01088](#)].
- [41] M. Seymour, *Jet shapes in hadron collisions: Higher orders, resummation and hadronization*, *Nucl.Phys.* **B513** (1998) 269–300, [[hep-ph/9707338](#)].
- [42] H.-n. Li, Z. Li, and C.-P. Yuan, *QCD resummation for jet substructures*, *Phys.Rev.Lett.* **107** (2011) 152001, [[arXiv:1107.4535](#)].
- [43] A. J. Larkoski, *QCD Analysis of the Scale-Invariance of Jets*, *Phys.Rev.* **D86** (2012) 054004, [[arXiv:1207.1437](#)].
- [44] M. Jankowiak and A. J. Larkoski, *Angular Scaling in Jets*, *JHEP* **1204** (2012) 039, [[arXiv:1201.2688](#)].

- [45] Y.-T. Chien and I. Vitev, *Jet Shape Resummation Using Soft-Collinear Effective Theory*, *JHEP* **1412** (2014) 061, [[arXiv:1405.4293](#)].
- [46] Y.-T. Chien, *Resummation of Jet Shapes and Extracting Properties of the Quark-Gluon Plasma*, *Int.J.Mod.Phys.Conf.Ser.* **37** (2015) 1560047, [[arXiv:1411.0741](#)].
- [47] J. Isaacson, H.-n. Li, Z. Li, and C. P. Yuan, *Factorization for substructures of boosted Higgs jets*, [arXiv:1505.06368](#).
- [48] D. Krohn, M. D. Schwartz, T. Lin, and W. J. Waalewijn, *Jet Charge at the LHC*, *Phys.Rev.Lett.* **110** (2013), no. 21 212001, [[arXiv:1209.2421](#)].
- [49] W. J. Waalewijn, *Calculating the Charge of a Jet*, *Phys.Rev.* **D86** (2012) 094030, [[arXiv:1209.3019](#)].
- [50] A. J. Larkoski, I. Moult, and D. Neill, *Toward Multi-Differential Cross Sections: Measuring Two Angularities on a Single Jet*, *JHEP* **1409** (2014) 046, [[arXiv:1401.4458](#)].
- [51] M. Procura, W. J. Waalewijn, and L. Zeune, *Resummation of Double-Differential Cross Sections and Fully-Unintegrated Parton Distribution Functions*, *JHEP* **1502** (2015) 117, [[arXiv:1410.6483](#)].
- [52] D. Bertolini, J. Thaler, and J. R. Walsh, *The First Calculation of Fractional Jets*, *JHEP* **1505** (2015) 008, [[arXiv:1501.01965](#)].
- [53] B. Bhattacharjee, S. Mukhopadhyay, M. M. Nojiri, Y. Sakaki, and B. R. Webber, *Associated jet and subjet rates in light-quark and gluon jet discrimination*, *JHEP* **1504** (2015) 131, [[arXiv:1501.04794](#)].
- [54] A. J. Larkoski, I. Moult, and D. Neill, *Analytic Boosted Boson Discrimination*, *JHEP* **05** (2016) 117, [[arXiv:1507.03018](#)].
- [55] M. Dasgupta, L. Schunk, and G. Soyez, *Jet shapes for boosted jet two-prong decays from first-principles*, *JHEP* **04** (2016) 166, [[arXiv:1512.00516](#)].
- [56] C. Frye, A. J. Larkoski, M. D. Schwartz, and K. Yan, *Precision physics with pile-up insensitive observables*, [arXiv:1603.06375](#).
- [57] C. Frye, A. J. Larkoski, M. D. Schwartz, and K. Yan, *Factorization for groomed jet substructure beyond the next-to-leading logarithm*, *JHEP* **07** (2016) 064, [[arXiv:1603.09338](#)].
- [58] Z.-B. Kang, F. Ringer, and I. Vitev, *Jet substructure using semi-inclusive jet functions within SCET*, [arXiv:1606.07063](#).
- [59] A. Hornig, Y. Makris, and T. Mehen, *Jet Shapes in Dijet Events at the LHC in SCET*, *JHEP* **04** (2016) 097, [[arXiv:1601.01319](#)].
- [60] S. Marzani, L. Schunk, and G. Soyez, *A study of jet mass distributions with grooming*, [arXiv:1704.02210](#).
- [61] S. Marzani, L. Schunk, and G. Soyez, *The jet mass distribution after Soft Drop*, [arXiv:1712.05105](#).
- [62] A. H. Hoang, S. Mantry, A. Pathak, and I. W. Stewart, *Extracting a Short Distance Top Mass with Light Grooming*, [arXiv:1708.02586](#).



- [63] A. J. Larkoski, I. Moult, and D. Neill, *Factorization and Resummation for Groomed Multi-Prong Jet Shapes*, [arXiv:1710.00014](#).
- [64] A. J. Larkoski, I. Moult, and D. Neill, *Analytic Boosted Boson Discrimination at the Large Hadron Collider*, [arXiv:1708.06760](#).
- [65] J. R. Walsh and S. Zuberi, *Factorization Constraints on Jet Substructure*, [arXiv:1110.5333](#).
- [66] A. J. Larkoski, I. Moult, and D. Neill, *Power Counting to Better Jet Observables*, *JHEP* **1412** (2014) 009, [[arXiv:1409.6298](#)].
- [67] A. J. Larkoski, I. Moult, and D. Neill, *Building a Better Boosted Top Tagger*, *Phys.Rev.* **D91** (2015), no. 3 034035, [[arXiv:1411.0665](#)].
- [68] J. Cogan, M. Kagan, E. Strauss, and A. Schwartzman, *Jet-Images: Computer Vision Inspired Techniques for Jet Tagging*, *JHEP* **02** (2015) 118, [[arXiv:1407.5675](#)].
- [69] L. de Oliveira, M. Kagan, L. Mackey, B. Nachman, and A. Schwartzman, *Jet-images — deep learning edition*, *JHEP* **07** (2016) 069, [[arXiv:1511.05190](#)].
- [70] L. G. Almeida, M. Backović, M. Cliche, S. J. Lee, and M. Perelstein, *Playing Tag with ANN: Boosted Top Identification with Pattern Recognition*, *JHEP* **07** (2015) 086, [[arXiv:1501.05968](#)].
- [71] P. Baldi, K. Bauer, C. Eng, P. Sadowski, and D. Whiteson, *Jet Substructure Classification in High-Energy Physics with Deep Neural Networks*, *Phys. Rev.* **D93** (2016), no. 9 094034, [[arXiv:1603.09349](#)].
- [72] D. Guest, J. Collado, P. Baldi, S.-C. Hsu, G. Urban, and D. Whiteson, *Jet Flavor Classification in High-Energy Physics with Deep Neural Networks*, [arXiv:1607.08633](#).
- [73] J. S. Conway, R. Bhaskar, R. D. Erbacher, and J. Pilot, *Identification of High-Momentum Top Quarks, Higgs Bosons, and W and Z Bosons Using Boosted Event Shapes*, [arXiv:1606.06859](#).
- [74] J. Barnard, E. N. Dawe, M. J. Dolan, and N. Rajcic, *Parton Shower Uncertainties in Jet Substructure Analyses with Deep Neural Networks*, [arXiv:1609.00607](#).
- [75] A. Abdesselam, E. B. Kuutmann, U. Bitenc, G. Brooijmans, J. Butterworth, et al., *Boosted objects: A Probe of beyond the Standard Model physics*, *Eur.Phys.J.* **C71** (2011) 1661, [[arXiv:1012.5412](#)].
- [76] A. Altheimer, S. Arora, L. Asquith, G. Brooijmans, J. Butterworth, et al., *Jet Substructure at the Tevatron and LHC: New results, new tools, new benchmarks*, *J.Phys.* **G39** (2012) 063001, [[arXiv:1201.0008](#)].
- [77] A. Altheimer, A. Arce, L. Asquith, J. Backus Mayes, E. Bergeaas Kuutmann, et al., *Boosted objects and jet substructure at the LHC. Report of BOOST2012, held at IFIC Valencia, 23rd-27th of July 2012*, *Eur.Phys.J.* **C74** (2014) 2792, [[arXiv:1311.2708](#)].
- [78] D. Adams et al., *Towards an Understanding of the Correlations in Jet Substructure*, *Eur. Phys. J.* **C75** (2015), no. 9 409, [[arXiv:1504.00679](#)].
- [79] A. J. Larkoski, I. Moult, and B. Nachman, *Jet Substructure at the Large Hadron Collider: A Review of Recent Advances in Theory and Machine Learning*, [arXiv:1709.04464](#).
- [80] A. J. Larkoski, G. P. Salam, and J. Thaler, *Energy Correlation Functions for Jet Substructure*, *JHEP* **1306** (2013) 108, [[arXiv:1305.0007](#)].

- [81] I. Moutl, L. Necib, and J. Thaler, *New Angles on Energy Correlation Functions*, *JHEP* **12** (2016) 153, [[arXiv:1609.07483](#)].
- [82] P. T. Komiske, E. M. Metodiev, and J. Thaler, *Energy flow polynomials: A complete linear basis for jet substructure*, [arXiv:1712.07124](#).
- [83] J. Thaler and K. Van Tilburg, *Identifying Boosted Objects with  $N$ -subjettiness*, *JHEP* **1103** (2011) 015, [[arXiv:1011.2268](#)].
- [84] J. Thaler and K. Van Tilburg, *Maximizing Boosted Top Identification by Minimizing  $N$ -subjettiness*, *JHEP* **1202** (2012) 093, [[arXiv:1108.2701](#)].
- [85] A. J. Larkoski, S. Marzani, G. Soyez, and J. Thaler, *Soft Drop*, *JHEP* **1405** (2014) 146, [[arXiv:1402.2657](#)].
- [86] D. Krohn, J. Thaler, and L.-T. Wang, *Jet Trimming*, *JHEP* **1002** (2010) 084, [[arXiv:0912.1342](#)].
- [87] J. Dolen, P. Harris, S. Marzani, S. Rappoccio, and N. Tran, *Thinking outside the ROCs: Designing Decorrelated Taggers (DDT) for jet substructure*, *JHEP* **05** (2016) 156, [[arXiv:1603.00027](#)].
- [88] G. P. Salam, L. Schunk, and G. Soyez, *Dichroic subjettiness ratios to distinguish colour flows in boosted boson tagging*, *JHEP* **03** (2017) 022, [[arXiv:1612.03917](#)].
- [89] T. Sjostrand, S. Mrenna, and P. Z. Skands, *PYTHIA 6.4 Physics and Manual*, *JHEP* **0605** (2006) 026, [[hep-ph/0603175](#)].
- [90] T. Sjostrand, S. Mrenna, and P. Z. Skands, *A Brief Introduction to PYTHIA 8.1*, *Comput.Phys.Commun.* **178** (2008) 852–867, [[arXiv:0710.3820](#)].
- [91] Y. L. Dokshitzer, G. Marchesini, and B. R. Webber, *Dispersive approach to power behaved contributions in QCD hard processes*, *Nucl. Phys.* **B469** (1996) 93–142, [[hep-ph/9512336](#)].
- [92] Y. L. Dokshitzer and B. Webber, *Calculation of power corrections to hadronic event shapes*, *Phys.Lett.* **B352** (1995) 451–455, [[hep-ph/9504219](#)].
- [93] G. P. Korchemsky and G. F. Sterman, *Power corrections to event shapes and factorization*, *Nucl.Phys.* **B555** (1999) 335–351, [[hep-ph/9902341](#)].
- [94] G. Korchemsky and S. Tafat, *On power corrections to the event shape distributions in QCD*, *JHEP* **0010** (2000) 010, [[hep-ph/0007005](#)].
- [95] S. Bosch, B. Lange, M. Neubert, and G. Paz, *Factorization and shape function effects in inclusive  $B$  meson decays*, *Nucl.Phys.* **B699** (2004) 335–386, [[hep-ph/0402094](#)].
- [96] A. H. Hoang and I. W. Stewart, *Designing gapped soft functions for jet production*, *Phys.Lett.* **B660** (2008) 483–493, [[arXiv:0709.3519](#)].
- [97] Z. Ligeti, I. W. Stewart, and F. J. Tackmann, *Treating the  $b$  quark distribution function with reliable uncertainties*, *Phys.Rev.* **D78** (2008) 114014, [[arXiv:0807.1926](#)].
- [98] I. W. Stewart, F. J. Tackmann, and W. J. Waalewijn, *Dissecting Soft Radiation with Factorization*, *Phys.Rev.Lett.* **114** (2015), no. 9 092001, [[arXiv:1405.6722](#)].
- [99] M. Cacciari, G. P. Salam, and S. Sapeta, *On the characterisation of the underlying event*, *JHEP* **04** (2010) 065, [[arXiv:0912.4926](#)].



- [100] **CMS Collaboration**, A. M. Sirunyan et al., *Inclusive search for a highly boosted Higgs boson decaying to a bottom quark-antiquark pair*, [arXiv:1709.05543](#).
- [101] **CMS Collaboration**, *Inclusive search for the standard model Higgs boson produced in pp collisions at  $\sqrt{s} = 13$  TeV using  $H \rightarrow b\bar{b}$  decays*, Tech. Rep. CMS-PAS-HIG-17-010, CERN, Geneva, 2017.
- [102] **CMS Collaboration**, *Search for light vector resonances decaying to a quark pair produced in association with a jet in proton-proton collisions at  $\sqrt{s} = 13$  TeV*, Tech. Rep. CMS-PAS-EXO-17-001, CERN, Geneva, 2017.
- [103] **CMS Collaboration**, A. M. Sirunyan et al., *Search for Low Mass Vector Resonances Decaying to Quark-Antiquark Pairs in Proton-Proton Collisions at  $\sqrt{s} = 13$  TeV*, *Phys. Rev. Lett.* **119** (2017), no. 11 111802, [[arXiv:1705.10532](#)].
- [104] **CMS Collaboration**, A. M. Sirunyan et al., *Search for low mass vector resonances decaying into quark-antiquark pairs in proton-proton collisions at  $\sqrt{s} = 13$  TeV*, [arXiv:1710.00159](#).
- [105] **ATLAS Collaboration**, M. Aaboud et al., *Search for light resonances decaying to boosted quark pairs and produced in association with a photon or a jet in proton-proton collisions at  $\sqrt{s} = 13$  TeV with the ATLAS detector*, [arXiv:1801.08769](#).
- [106] C. Shimmin, P. Sadowski, P. Baldi, E. Weik, D. Whiteson, E. Goul, and A. Sogaard, *Decorrelated Jet Substructure Tagging using Adversarial Neural Networks*, *Phys. Rev.* **D96** (2017), no. 7 074034, [[arXiv:1703.03507](#)].
- [107] J. A. Aguilar-Saavedra, J. H. Collins, and R. K. Mishra, *A generic anti-QCD jet tagger*, *JHEP* **11** (2017) 163, [[arXiv:1709.01087](#)].
- [108] I. Mout, B. Nachman, and D. Neill, *Convolved Substructure: Analytically Decorrelating Jet Substructure Observables*, [arXiv:1710.06859](#).
- [109] I. W. Stewart, F. J. Tackmann, and W. J. Waalewijn, *N-Jettiness: An Inclusive Event Shape to Veto Jets*, *Phys.Rev.Lett.* **105** (2010) 092002, [[arXiv:1004.2489](#)].
- [110] I. W. Stewart, F. J. Tackmann, J. Thaler, C. K. Vermilion, and T. F. Wilkason, *XCone: N-jettiness as an Exclusive Cone Jet Algorithm*, *JHEP* **11** (2015) 072, [[arXiv:1508.01516](#)].
- [111] S. Catani, Y. L. Dokshitzer, M. Seymour, and B. Webber, *Longitudinally invariant  $K_t$  clustering algorithms for hadron hadron collisions*, *Nucl.Phys.* **B406** (1993) 187–224.
- [112] A. J. Larkoski, D. Neill, and J. Thaler, *Jet Shapes with the Broadening Axis*, *JHEP* **1404** (2014) 017, [[arXiv:1401.2158](#)].
- [113] M. Cacciari, G. P. Salam, and G. Soyez, *FastJet User Manual*, *Eur.Phys.J.* **C72** (2012) 1896, [[arXiv:1111.6097](#)].
- [114] A. J. Larkoski and I. Mout, *The Singular Behavior of Jet Substructure Observables*, *Phys. Rev.* **D93** (2016) 014017, [[arXiv:1510.08459](#)].
- [115] S. Catani, G. Turnock, and B. Webber, *Jet broadening measures in  $e^+e^-$  annihilation*, *Phys.Lett.* **B295** (1992) 269–276.
- [116] Y. L. Dokshitzer, A. Lucenti, G. Marchesini, and G. Salam, *On the QCD analysis of jet broadening*, *JHEP* **9801** (1998) 011, [[hep-ph/9801324](#)].

- [117] A. Banfi, G. P. Salam, and G. Zanderighi, *Principles of general final-state resummation and automated implementation*, *JHEP* **0503** (2005) 073, [[hep-ph/0407286](#)].
- [118] J. M. Butterworth, A. R. Davison, M. Rubin, and G. P. Salam, *Jet substructure as a new Higgs search channel at the LHC*, *Phys.Rev.Lett.* **100** (2008) 242001, [[arXiv:0802.2470](#)].
- [119] S. D. Ellis, C. K. Vermilion, and J. R. Walsh, *Techniques for improved heavy particle searches with jet substructure*, *Phys.Rev.* **D80** (2009) 051501, [[arXiv:0903.5081](#)].
- [120] S. D. Ellis, C. K. Vermilion, and J. R. Walsh, *Recombination Algorithms and Jet Substructure: Pruning as a Tool for Heavy Particle Searches*, *Phys.Rev.* **D81** (2010) 094023, [[arXiv:0912.0033](#)].
- [121] M. Cacciari, G. P. Salam, and G. Soyez, *The Anti- $k(t)$  jet clustering algorithm*, *JHEP* **0804** (2008) 063, [[arXiv:0802.1189](#)].
- [122] Y. L. Dokshitzer, G. Leder, S. Moretti, and B. Webber, *Better jet clustering algorithms*, *JHEP* **9708** (1997) 001, [[hep-ph/9707323](#)].
- [123] M. Wobisch and T. Wengler, *Hadronization corrections to jet cross-sections in deep inelastic scattering*, [hep-ph/9907280](#).
- [124] M. Wobisch, *Measurement and QCD analysis of jet cross-sections in deep inelastic positron proton collisions at  $\sqrt{s} = 300$  GeV*, 2000.
- [125] A. J. Larkoski and J. Thaler, *Unsafe but Calculable: Ratios of Angularities in Perturbative QCD*, *JHEP* **1309** (2013) 137, [[arXiv:1307.1699](#)].
- [126] A. J. Larkoski, S. Marzani, and J. Thaler, *Sudakov Safety in Perturbative QCD*, *Phys.Rev.* **D91** (2015), no. 11 111501, [[arXiv:1502.01719](#)].
- [127] M. Dasgupta and G. Salam, *Resummation of nonglobal QCD observables*, *Phys.Lett.* **B512** (2001) 323–330, [[hep-ph/0104277](#)].
- [128] Y. Gao, A. V. Griksan, Z. Guo, K. Melnikov, M. Schulze, and N. V. Tran, *Spin determination of single-produced resonances at hadron colliders*, *Phys. Rev.* **D81** (2010) 075022, [[arXiv:1001.3396](#)].
- [129] S. Bolognesi, Y. Gao, A. V. Griksan, K. Melnikov, M. Schulze, N. V. Tran, and A. Whitbeck, *On the spin and parity of a single-produced resonance at the LHC*, *Phys. Rev.* **D86** (2012) 095031, [[arXiv:1208.4018](#)].
- [130] B. Andersson, G. Gustafson, L. Lonnblad, and U. Pettersson, *Coherence Effects in Deep Inelastic Scattering*, *Z. Phys.* **C43** (1989) 625.
- [131] B. Andersson, G. Gustafson, G. Ingelman, and T. Sjostrand, *Parton Fragmentation and String Dynamics*, *Phys. Rept.* **97** (1983) 31–145.
- [132] B. Andersson, *The Lund model*, *Camb. Monogr. Part. Phys. Nucl. Phys. Cosmol.* **7** (1997) 1–471.
- [133] B. R. Webber, *A QCD Model for Jet Fragmentation Including Soft Gluon Interference*, *Nucl. Phys.* **B238** (1984) 492–528.
- [134] G. Marchesini and B. R. Webber, *Monte Carlo Simulation of General Hard Processes with Coherent QCD Radiation*, *Nucl. Phys.* **B310** (1988) 461–526.

- [135] A. Buckley, J. Butterworth, S. Gieseke, D. Grellscheid, S. Hoche, et al., *General-purpose event generators for LHC physics*, *Phys.Rept.* **504** (2011) 145–233, [[arXiv:1101.2599](#)].
- [136] P. Z. Skands, *QCD for Collider Physics*, in *Proceedings, High-energy Physics. Proceedings, 18th European School (ESHEP 2010): Raseborg, Finland, June 20 - July 3, 2010*, 2011. [arXiv:1104.2863](#).
- [137] P. Skands, *Introduction to QCD*, [arXiv:1207.2389](#).
- [138] ATLAS Collaboration, *The ATLAS Experiment at the CERN Large Hadron Collider*, *JINST* **3** (2008) S08003.
- [139] CMS Collaboration, *The CMS experiment at the CERN LHC*, *JINST* **3** (2008) S08004.
- [140] M. Cacciari and G. P. Salam, *Pileup subtraction using jet areas*, *Phys. Lett.* **B659** (2008) 119–126, [[arXiv:0707.1378](#)].
- [141] R. Alon, E. Duchovni, G. Perez, A. P. Pranko, and P. K. Sinervo, *A Data-driven method of pile-up correction for the substructure of massive jets*, *Phys. Rev.* **D84** (2011) 114025, [[arXiv:1101.3002](#)].
- [142] G. Soyez, G. P. Salam, J. Kim, S. Dutta, and M. Cacciari, *Pileup subtraction for jet shapes*, *Phys.Rev.Lett.* **110** (2013), no. 16 162001, [[arXiv:1211.2811](#)].
- [143] J. Tseng and H. Evans, *Sequential recombination algorithm for jet clustering and background subtraction*, *Phys. Rev.* **D88** (2013) 014044, [[arXiv:1304.1025](#)].
- [144] D. Krohn, M. D. Schwartz, M. Low, and L.-T. Wang, *Jet Cleansing: Pileup Removal at High Luminosity*, *Phys. Rev.* **D90** (2014), no. 6 065020, [[arXiv:1309.4777](#)].
- [145] M. Cacciari, G. P. Salam, and G. Soyez, *SoftKiller, a particle-level pileup removal method*, *Eur. Phys. J.* **C75** (2015), no. 2 59, [[arXiv:1407.0408](#)].
- [146] D. Bertolini, P. Harris, M. Low, and N. Tran, *Pileup Per Particle Identification*, *JHEP* **10** (2014) 059, [[arXiv:1407.6013](#)].
- [147] M. Cacciari, G. P. Salam, and G. Soyez, *The Catchment Area of Jets*, *JHEP* **04** (2008) 005, [[arXiv:0802.1188](#)].
- [148] A. J. Larkoski and J. Thaler, *Aspects of jets at 100 TeV*, *Phys.Rev.* **D90** (2014), no. 3 034010, [[arXiv:1406.7011](#)].